Geochemistry, Geophysics, Geosystems®

AGU ADVANCING EARTH AND SPACE SCIENCES

RESEARCH ARTICLE
10.1029/2026GC012942

Interface Deformation, Exhumation, and Underplating: The Role of Plate Velocity Changes Throughout the Evolution of a Subduction Zone

Valeria Turino[1,2], **Adam F. Holt**[1], **Derek J. Neuharth**[3,4], **Ryan K. Stoner**[1,5], and **Whitney M. Behr**[3]

[1]Rosenstiel School of Marine, Atmospheric, and Earth Science, University of Miami, Miami, FL, USA, [2]Department of Geosciences, The Pennsylvania State University, University Park, PA, USA, [3]Geological Institute, ETH Zürich, Zurich, Switzerland, [4]GFZ German Research Centre for Geosciences, Potsdam, Germany, [5]Department of Earth and Climate Sciences, Tufts University, Medford, TX, USA

Abstract Exhumed metamorphic rocks yield critical insights into the mechanical, chemical, and thermal structure of the plate interface that can be used to infer exhumation pathways and their evolution throughout a subduction zone's lifetime. Metamorphosed oceanic rocks often record exhumation and underplating over relatively punctuated time periods, which appear to be linked to specific stages of subduction. Although plate velocities also vary from one stage of subduction to the next, the influence of this time dependence on exhumation and underplating remains unclear. We therefore use 2-D time-dependent subduction models to investigate how evolving plate velocities affect the timing and distribution of exhumation and underplating. By extracting plate velocities from a freely evolving subduction model and imposing them on kinematically driven models, we isolate the effects of realistic velocity variations on interface processes without the complexity of a dynamically evolving slab. We also explore the role of interface strength by varying its rheology and composition. In our models, exhumation consistently initiates during a punctuated detachment event following decreases in subduction velocity. Shallow exhumation (<50 km) occurs through corner flow within the accretionary prism, while deeper underplating (<140 km) involves crustal slicing and detachment along the whole interface. Weak interfaces favor continuous and voluminous exhumation, whereas strong interfaces restrict it to brief, punctuated episodes. Underplating is discontinuous throughout but increases in volume as convergence slows. These findings demonstrate that time-dependent plate velocity variations exert significant control on interface processes and naturally generate punctuated exhumation and underplating consistent with the rock record.

Plain Language Summary Exhumation and underplating of rocks in oceanic subduction zones, which happen discontinuously during a subduction zone's lifetime, are still not fully understood. Despite many efforts, the timing of rock recovery during the evolution of a subduction zone remains unclear. In this study, we use a model to simulate how typical changes in plate speed and strength of the plate interface influence exhumation and underplating. Our results show that both processes vary in time and depend on evolving plate velocities. During exhumation, rocks detach from the slab in a single event and are then transported upwards into the accretionary wedge. Stagnation of rocks can also occur along the entire plate interface through repeated slicing of portions of the slab. When the plate interface is weak, exhumation is more continuous, while strong interfaces lead to less frequent exhumation. Stagnation is always discontinuous, independently from the properties of the interface. These findings show how changes in plate movement and interface strength influence exhumation and stagnation, offering new insights into the role of plate velocity in controlling the exhumation and underplating of rocks.

Key Points:

- Subduction models show that time-evolving plate velocities exert significant control on the timing of exhumation and underplating
- Exhumed material detaches from the slab in a single event after subduction slowdown, with exhumation style modulated by interface rheology
- Underplating is episodic throughout subduction but increases in volume as convergence slows, occurring along the full interface

Supporting Information:

Supporting Information may be found in the online version of this article.

Correspondence to:

V. Turino and A. F. Holt,
valeria.turino@psu.edu;
aholt@miami.edu

Citation:

Turino, V., Holt, A. F., Neuharth, D. J., Stoner, R. K., & Behr, W. M. (2026). Interface deformation, exhumation, and underplating: The role of plate velocity changes throughout the evolution of a subduction zone. *Geochemistry, Geophysics, Geosystems*, *27*, e2026GC012942. https://doi.org/10.1029/2026GC012942

Received 5 FEB 2026
Accepted 15 JUN 2026

Author Contributions:

Conceptualization: Valeria Turino, Adam F. Holt
Data curation: Valeria Turino
Formal analysis: Valeria Turino
Funding acquisition: Adam F. Holt
Investigation: Valeria Turino, Adam F. Holt
Methodology: Valeria Turino, Adam F. Holt, Derek J. Neuharth, Ryan K. Stoner
Project administration: Adam F. Holt
Resources: Adam F. Holt

1. Introduction

Exhumed metamorphic rocks provide critical insights into the evolving thermal, mechanical, and chemical state of the plate interface. The *P–T* paths and deformation history of metamorphic rocks depend on the forces that drive plate interface deformation, such as the balance between rock buoyancy and viscous stresses at depth, which determine how and when exhumation and/or overprinting occur. Despite extensive field (e.g., Guillot et al., 2009; Jolivet et al., 2003; Platt, 1975) and modeling (e.g., Cloos, 1982; Gerya et al., 2002; Hacker & Gerya, 2013; Peacock, 1992) studies, the dominant mechanisms and timing of exhumation of high-pressure (HP) crustal rocks

Software: Valeria Turino, Derek J. Neuharth, Ryan K. Stoner
Supervision: Adam F. Holt, Derek J. Neuharth, Whitney M. Behr
Validation: Valeria Turino, Adam F. Holt, Derek J. Neuharth
Visualization: Valeria Turino
Writing – original draft: Valeria Turino, Adam F. Holt, Derek J. Neuharth, Ryan K. Stoner, Whitney M. Behr
Writing – review & editing: Valeria Turino, Adam F. Holt, Derek J. Neuharth, Ryan K. Stoner, Whitney M. Behr

throughout the lifetime of an oceanic subduction zone remain debated. Unlike the relatively buoyant HP and ultrahigh-pressure (UHP) rocks that exhume during continental collision (Ernst et al., 1997), denser oceanic rocks, such as eclogites, require additional forces and/or mixing with positively buoyant material to overcome both their excess density and the down-dragging shear force exerted by the sinking slab (England & Holland, 1979; Ernst, 1975).

The rock record indicates that the exhumation of oceanic HP rocks is relatively short-lived, or "punctuated," with respect to a subduction zone's lifetime (e.g., Agard et al., 2009; Bellot & Roig, 2007; Krohe & Mposkos, 2002). The early phase of rock exhumation—from slab detachment to exhumation to mid-crustal levels—can involve multiple mechanisms operating at different depths, including corner flow in the shallow accretionary prism (≤50 km, Cloos, 1982; Shreve & Cloos, 1986), return flow in the deeper subduction channel (≤80 km, Jolivet et al., 2003; Federico et al., 2007), and multi-stage exhumation via underplating or transient stalling before final ascent (Moore, 1989; Poulaki et al., 2019; Tewksbury-Christle et al., 2021). Yet, irrespective of the mechanism, the causes of this punctuated behavior are debated. Variations in plate interface strength and buoyancy, which evolve in time with temperature, lithology, and/or fluid availability (Abila et al., 2025; Bebout & Penniston-Dorland, 2016; Dragovic et al., 2020; Krebs et al., 2011; Muñoz-Montecinos et al., 2021), may contribute to exhumation and tectonic slicing (Menant et al., 2019). Preferential exhumation may also occur during inherently time-dependent tectonic "events" such as slab break-off, rollback, overriding plate extension (Fassoulas et al., 1994; Garrido et al., 2011; Maruyama & Parkinson, 2000), or the initiation and/or termination of subduction (Bermúdez et al., 2017; Ring et al., 2007; Rubatto & Scambelluri, 2003; van Keken et al., 2018; Wang et al., 2023). Subduction initiation or termination are characterized by low subducting plate speeds, which may aid the rise of high-pressure rocks by reducing the down-dip directed shear stress at the base of the plate interface (Ernst, 1975). However, exhumed rocks in the geologic record do not appear limited to these tectonic events (e.g., Agard et al., 2018), suggesting the importance of additional factors. Moreover, plate speed variability is not limited to the initial and terminal phases of subduction; both tectonic reconstructions (e.g., Croon et al., 2008; Sdrolias & Müller, 2006) and dynamic subduction models (e.g., Cerpa et al., 2014; Enns et al., 2005), show that plate velocities can change significantly over a few million years. Yet, the extent to which these less drastic plate velocity changes influence exhumation and underplating is poorly understood.

Previous modeling studies have investigated the mechanisms responsible for HP exhumation within oceanic subduction zones mainly using two approaches: (a) models that incorporate evolving plate interface geometries and various rheological weakening mechanisms, often tied to specific lithologies, and (b) models that explore the effects of variable plate velocities in more simplified or analytical setups. In the former, exhumation is primarily facilitated by internal interface weakening mechanisms, such as fluid release and serpentinization, which enable the formation of a buoyant and weak subduction channel (Burov et al., 2001; Gerya et al., 2002; Gorczyk et al., 2007; Malatesta et al., 2012; Vaughan-Hammon et al., 2022; Wang et al., 2019) or facilitate tectonic slicing and subsequent exhumation (Angiboust et al., 2012; Menant et al., 2019; Ruh et al., 2015). Such models, with typically constant plate velocities, produce sustained or long-lasting exhumation persisting throughout convergence, sometimes involving transient stalling at crustal depths before the final ascent of exhumed material. However, this near-continuous exhumation appears at odds with the punctuated rock record. The impact of plate velocity changes, as described above, has mainly been explored with the second type of modeling approach; analytical models of plate interface deformation. Instead of simulating the full evolution of the subduction system, such studies typically focus on dramatic plate velocity changes, as associated with events likes slab break-off or subduction cessation (England & Holland, 1979; Ernst, 1970, 1975, 1988; Platt, 1993). For example, recent analytical modeling by England and Smye (2023), which considers non-Newtonian and temperature-dependent viscous deformation within subduction channels, argues that significant exhumation from >50 km depth occurs only in response to a major reduction in subduction rate and the associated reduction in the down-dip shear stress at the base of the channel. While such analytical approaches offer fundamental insightful, the coupled impact of more moderate time-dependent slowdowns and gradual changes in plate interface structure, necessitates a numerical modeling approach.

Here we use numerical subduction models to investigate the relationship between time-dependent plate velocity and plate interface deformation, including the timing, distribution, and volume of exhumation and underplating. We aim to develop a geodynamic baseline for what exhumation behavior emerges naturally during the lifetime of an idealized oceanic subduction zone versus what likely requires additional complexities, such as abrupt tectonic "events" that may be unique to individual subduction systems. We also isolate the effects of interface strength by

comparing "strong" and "weak" plate interfaces and examine the impact of preexisting abyssal serpentinization at the base of the oceanic crust. Within our models, exhumation and underplating occur preferentially at subduction stages that are characterized by temporal changes in plate velocities. All exhumed material within our models detaches from the slab during one punctuated event, after a slowdown from the most rapid subduction rates, while subsequent exhumation paths vary based on the interface rheology. These findings align with the geological record of punctuated HP exhumation, illuminating how evolving plate velocities impact plate interface deformation throughout the lifetime of subduction zones.

2. Methods

2.1. Modeling Strategy and Governing Equations

We set up subduction models using the ASPECT geodynamic modeling code, v.2.6.0-pre (Bangerth et al., 2023; Gassmöller et al., 2018; Heister et al., 2017; Kronbichler et al., 2012; Rose et al., 2017) and adopt a kinematically driven approach within which we impose a time-dependent plate velocity evolution on both the subducting and overriding plates (Figure 1b). This approach allows us to test the impact of time-evolving plate velocities on exhumation and underplating processes. Our subducting plate contains an oceanic crust overlain by a sedimentary layer; the oceanic crust is composed of a single layer of basalts (i.e., unaltered oceanic crust), which transforms into eclogite (i.e., eclogitized oceanic crust) at high pressure. Each model composition is characterized by distinct densities and rheological constitutive laws (detailed in Section 2.3). As the bulk viscous strength of plate interfaces is likely to exhibit at least an order of magnitude variation between Earth's subduction zones–as a function of temperature, lithology, and fluid content (e.g., Abila et al., 2025; Bebout & Penniston-Dorland, 2016; Behr & Becker, 2018)–we also run models with relatively weak versus relatively strong interfaces. Throughout this paper, we refer to the plate interface as the finite-width region bound by the rigid portions of the subducting and overriding plates. In this context, the interface represents a domain composed of both the accretionary wedge and the assemblage of oceanic crust, sediments, and eclogites within the subduction channel, including the evolving main shear zone. This definition clarifies that "thickening" or "motion" of the interface refers to the evolution of this heterogeneous material layer rather than a singular boundary plane.

Dynamic subduction models exhibit plate velocities that evolve depending on the phase of subduction (e.g., Enns et al., 2005). Therefore, imposing constant plate velocities is inconsistent with our expectations of dynamically evolving subduction zones. For this reason, we impose a time-dependent plate velocity evolution that we extract from a separate, dynamic subduction model with the same initial geometry (Figure S1 in Supporting Information S1). That is, a model without imposed velocities or forces, in which an oceanic subducting plate (SP) sinks under a continental overriding plate (OP), and plate velocities self-consistently evolve in response to the subduction zone force balance. Specifically, we extract the convergence velocity (or rate), which is the relative velocity between the two plates, $v_c = v_{SP} - v_{OP}$. Because our overriding plate is modeled as a rigid mechanical barrier that does not plastically yield, the trench velocity is effectively equal to v_{OP}, so that v_c is also equivalent to the subduction velocity, $v_{SP} - v_{trench}$ (Lallemand et al., 2005). We use this same time-dependent velocity profile for each of the kinematically driven models, enabling an evolving plate velocity structure that encapsulates variable phases of subduction. This approach ensures that our plate velocity evolution mimics the time-dependent phases of subduction, such as the dynamic slowdown as the slab reaches the lower mantle, while providing a controlled kinematic framework to isolate the influence of velocity on exhumation and underplating.

Within this framework, ASPECT is used to solve the equations for the conservation of mass (Equation 1), momentum (Equation 2), and energy (Equation 3) for an incompressible Boussinesq fluid with no inertia and no shear heating:

$$\nabla \cdot \mathbf{v} = 0 \tag{1}$$

$$-\nabla \cdot 2\eta\dot{\varepsilon} + \nabla P = \rho\mathbf{g} \tag{2}$$

$$\rho C_p\left(\frac{\partial T}{\partial t} + \mathbf{v}\cdot\nabla T\right) - k\nabla^2 T = \rho H \tag{3}$$

Where $\mathbf{v}$ is velocity, η is viscosity, $\dot{\varepsilon}$ is strain rate, P is pressure, ρ is density, $\mathbf{g}$ is gravitational acceleration, C_p is specific heat capacity, T is temperature, and k is thermal conductivity (Table 1).

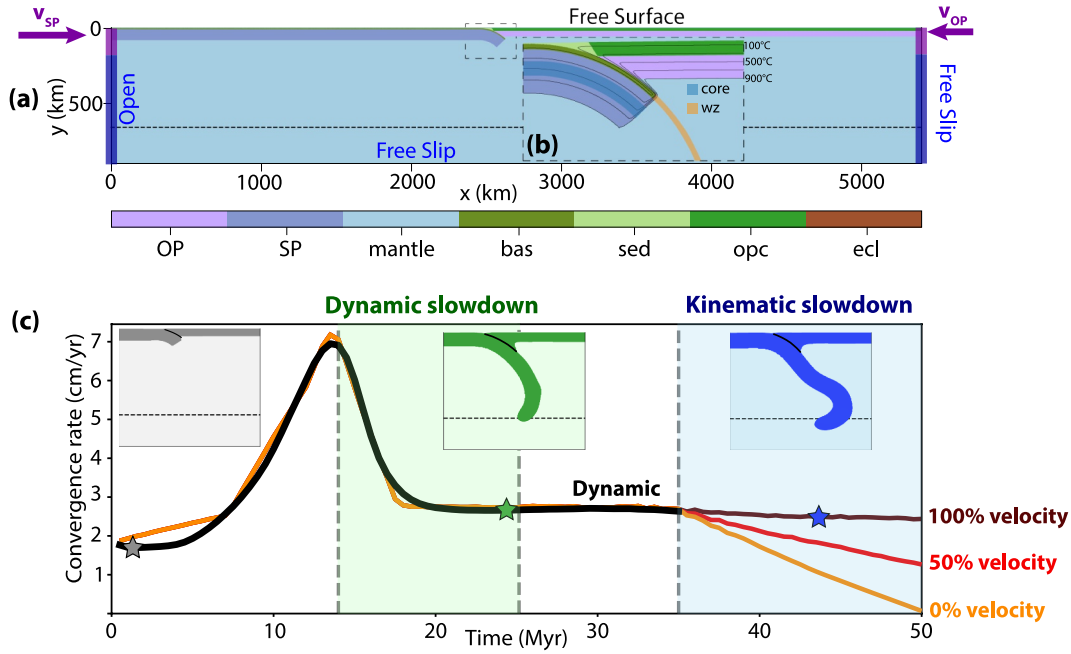

Figure 1. (a) Model setup, with a zoom-in of the plates structure and the boundary conditions: in blue we highlight the boundary conditions below the inflow zone, while in purple we show the applied velocities/inflow conditions applied to the lithosphere. The colorbar shows the five lithological components within the subducting and overriding plates (bas = basalt; sed = sediments, opc = overriding plate crust, ecl = eclogites) plus the mantle; within the mantle, the darker blue area shows a filled in contour of the subducting lithosphere (SP) as defined thermally, while in violet we show the overriding plate lithosphere (OP). (b) Shows the complete list of compositions, including the subducting plate strong core and the initial weak zone. The eclogites are not present at time $t = 0$ Myr, but develop at later times as the slab reaches the conditions for eclogite growth according to their phase diagram. (c) Velocity structure imposed on the lithospheric plates. The black line represents the extracted convergence rate from a ocean-continent dynamic model, the three red curves the velocities imposed on the kinematic models. The slab shape is shown for the times identified by the star symbol: beginning of the model run, end of dynamic slowdown and kinematic slowdown. The dashed line represents the upper-lower mantle boundary at 660 km of depth.

In addition to these equations, ASPECT tracks the movement of several compositions throughout the model, with each corresponding to distinct lithologies with physical properties that differ from those of the background mantle material. Advection of these compositions follows:

$$\frac{\partial C_i}{\partial t} + \mathbf{v} \cdot \nabla C_i = 0 \tag{4}$$

where C_i is compositional value for the i-th composition; C_i ranges from 0 to 1, where 0 indicates that the i-th compositional field is completely absent from a computational cell, and 1 that the cell is fully occupied by it. In our model, there are 7 distinct compositions, including basalt, sediments, and eclogites. For each composition, Equation 4 is solved using either the active particle method (Gassmöller et al., 2018) or the fields method (Bangerth et al., 2023), depending on the composition in question. This choice stems from the need to balance accuracy and efficiency in the models: the particle method (higher resolution, but more computationally expensive) is used to resolve and track the compositional fields within which we track exhumation within the subducting plate (sediments, basalts, eclogites), while the fields method is used for all other compositions to reduce computational cost. All compositions are described in detail in the following section.

2.2. Model Setup

We model oceanic subduction beneath a continental plate over 50 Myr in a 2-D, Cartesian domain. The domain has dimensions (x, y) = (5,400 km, 900 km) (Figure 1a), where 240 km of higher viscosity, lower mantle material

Table 1
List of Reference Mechanical Parameters With Values and Units

Parameter	Symbol	Value	Unit
Reference viscosity	η_{ref}	Mantle: 2.5 × 10^{20}	Pa s
		Strong core: 2.5 × 10^{20}	Pa s
		Weak zone, isoviscous: 2 × 10^{20}	Pa s
		Overriding lithosphere: 2.5 × 10^{20}	Pa s
		Continental crust, isoviscous: 2 × 10^{23}	Pa s
		Basalt: 5 × 10^{19}	Pa s
		Sediments: 1 × 10^{19}	Pa s
		Eclogite: 5 × 10^{20}	Pa s
		Serpentinite: 6 × 10^{18}	Pa s
Reference strain rate	$\dot{\varepsilon}$	9 × 10^{-13}	s^{-1}
Reference density	ρ_0	Mantle: 3,300	kg m^{-3}
		Strong core: 3,300	kg m^{-3}
		Weak zone: 3,500	kg m^{-3}
		Overriding lithosphere: 3,200	kg m^{-3}
		Continental crust: 2,700	kg m^{-3}
		Basalt 2,900	kg m^{-3}
		Sediments: 2,700	kg m^{-3}
		Eclogite: 3,400	kg m^{-3}
		Serpentinite: 2,700	kg m^{-3}
Pressure	P	–	Pa
Gravitational acceleration	$\mathbf{g}$	9.81	m s^{-2}
Specific heat capacity	C_p	940	J kg^{-1} K^{-1}
Surface temperature	T_s	0	°C
Mantle potential temperature	Tm	1421	°C
Adiabatic gradient		0.3	°/km
Thermal conductivity	k	3	W m^{-1} K^{-1}
Thermal diffusivity	κ	10^{-6}	m^2 s^{-1}
Thermal expansivity	α	3 × 10^{-5}	K^{-1}
Internal heat production	H_r	Background material: 0.022 × 10^{-6}[a]	W/m^3
		Subducting crust: 0.25 × 10^{-6}[a]	W/m^3
		Continental crust: 1.3 × 10^{-6}[b]	W/m^3

[a]Faccenda et al. (2008). [b]Syracuse et al. (2010).

is included to capture interactions between the slab and the upper-lower mantle viscosity jump at 660 km depth (e.g., Stegman et al., 2006).

The subducting oceanic lithosphere is initialized with a half-space cooling thermal profile that corresponds to a plate age of 90 Myr, while the overriding lithosphere is continental with an initially linear geotherm from the surface to the mantle temperature (1420°C) at the ~80 km base of the lithosphere. The overriding plate crust includes an internal heat production rate of $H_r = 1.3 \times 10^{-6}$ W/m^3 (Syracuse et al., 2010). The background material and oceanic crust have internal heating rates of, respectively, 0.022×10^{-6} W/m^3 and 0.25×10^{-6} W/m^3 (Faccenda et al., 2008). All model densities are temperature dependent, with different reference densities for individual compositions/lithologies (mantle and subducting plate lithosphere: 3300 kg/m^3; basalt: 2900 kg/m^3; sediments and overriding plate crust: 2700 kg/m^3; eclogite: 3400 kg/m^3; overriding plate lithospheric mantle: 3200 kg/m^3). The thermal boundary conditions for the top and bottom boundaries are constant temperature corresponding, respectively, to the surface temperature $T_{surf} = 0$°C and the

mantle temperature T_{mantle} = 1420°C. We fix the side boundaries to the initial lithospheric thermal structure: half-space cooling for a 90 Myr old subducting plate on the left and a linear geotherm for the overriding plate on the right.

As an idealized oceanic subduction zone crustal structure, we model, on top of the oceanic lithosphere, 7.5 km of basaltic crust overlain by 1 km of sediment. By adopting this simple architecture, typical of fast-spreading lithosphere type, we intentionally omit the lithological heterogeneities typical of slow-spreading systems (such as serpentinized slab mantle that separates mafic blocks and pre-cuts the slab), which facilitate exhumation (cf. Angiboust et al., 2012; Ruh et al., 2015). This approach allows us to isolate the first-order influence of time-dependent plate velocities on exhumation while providing a framework for understanding exhumation in systems lacking weak structural domains. We impose an initial proto-slab at the start of the model (Figure 1a), extending to 75 km depth, to aid with subduction initiation. We also include a sedimentary accretionary prism, down to an initial depth of 20 km and extending 75 km outboard of the trench (cf. Brizzi et al., 2021), whose shape and depth evolve during the model run (Figure 1a, Figure S2a in Supporting Information S1). The prism is included to provide an initially self-consistent distribution of sediments along the plate interface of the proto-slab (e.g., Ruh et al., 2015; Sizova et al., 2010). In the trench area, an 8.5 km thick initial weak zone is implemented to ensure the decoupling of the subducting and overriding plate during the first ~200 kyr of the model run, after which it is completely subducted (see weak zone geometry within Figure S2 in Supporting Information S1). The overriding plate includes a 20 km thick layer of strong crust, with a viscosity of 2×10^{23} Pa s, which prevents forearc erosion and continental crust subduction. This thickness is representative of thinned continental lithosphere in back-arc or margin settings; furthermore, given that plasticity is disabled and viscosity is capped at 2×10^{23} Pa s within the plate, the model dynamics are insensitive to variations in continental crustal thickness.

2.3. Rheology

The viscous rheology for each composition corresponds to diffusion and/or dislocation creep. Sediments, basalts, and eclogites are described solely through a dislocation creep flow law:

$$\eta_{disl} = \frac{1}{2} A_{disl}^{-\frac{1}{n}} \dot{\varepsilon}_{II}^{\frac{1-n}{n}} \exp\left(\frac{E_{disl} + PV_{disl}}{nRT}\right) \quad (5)$$

where A is a rheological prefactor, n the flow law exponent, $\dot{\varepsilon}$ the second invariant of the strain rate, E the activation energy, V the activation volume, T the temperature, and R the gas constant. Although our models are incompressible, we add an adiabatic temperature gradient of 0.3°C/km to the modeled temperature as a post-processing step (e.g., Van Keken et al., 2011). This value is consistent with established thermal benchmarks and allows for a more direct comparison between our numerical results and petrological P–T estimates. The prefactors are constants calculated by setting the viscosity to a prescribed constant value at a reference strain rate; the effective viscosities for each lithology, and therefore their material strength, then evolve over time according to the dependencies within the dislocation creep flow law (i.e., with the evolving strain rates, temperatures, and pressures). The reference strain rate is set to 9×10^{-13} s^{-1} for all crustal lithologies that corresponds to simple shear within. for example, a 3 km wide channel driven by a convergence rate of 10 cm/yr. At this strain rate, the prefactors are set to give reference viscosities of 10^{19} Pa s for the sediments, 5×10^{19} Pa s for the basalts, 5×10^{20} Pa s for the eclogite, and 6×10^{18} Pa s for the serpentinites. These values correspond to the effective viscosities of these lithologies at typical subduction interface temperatures of 327°C, following Behr and Becker's (2018) compilation of experimentally derived flow laws.

The upper mantle has a composite diffusion-dislocation creep flow with parameter values corresponding to dry olivine (Hirth & Kohlstedt, 2003). The dislocation creep viscosity follows Equation 5, and diffusion creep is:

$$\eta_{diff} = \frac{1}{2} A_{diff} \exp\left(\frac{E_{diff} + PV_{diff}}{RT}\right) \quad (6)$$

We assume a constant grain size of 1 mm (Hirth & Kohlstedt, 2003). Consequently, the pre-exponential factor A_{diff} accounts for this fixed grain size, and hence we do not consider grain-size evolution. The mantle diffusion and dislocation creep prefactors are set to produce $\eta_{diff} = \eta_{disl} = 5 \times 10^{20}$ Pa s at a reference strain rate of

10^{-15} s^{-1} and depth of 330 km; when harmonically averaged, these values produce an reference effective viscosity of 2.5 $\times$ 10^{20} Pa s. Because of the temperature dependence of the exponential term, this produces extremely high viscosities within the lithospheric plates; we therefore impose a maximum viscosity of 10^{23} Pa s for the background material and a maximum viscosity of 10^{24} Pa s within a strong, 20 km thick core of the subducting plate (Figure S2 in Supporting Information S1). Physically, these caps serve as a proxy for deformation mechanisms not explicitly modeled here, such as Peierls creep, which naturally limit the maximum stresses sustainable by the lithosphere at low temperatures. The lower mantle deforms only through diffusion creep, with an effective viscosity 30 times that of upper mantle diffusion creep.

Throughout the domain, composite diffusion-dislocation viscosities are computed as the harmonic mean of the diffusion and dislocation viscosities (with diffusion creep excluded for the crust and sediment):

$$\eta_{comp} = \left(\frac{1}{\eta_{diff}} + \frac{1}{\eta_{disl}}\right)^{-1} \tag{7}$$

and the model (effective) viscosities are limited by the plastic viscosity, such that:

$$\eta_{eff} = \min\left(\eta_{comp}, \eta_{yield}\right) \tag{8}$$

where the plastic yielding viscosity is added to simulate brittle/semi-brittle deformation at lithospheric depths. This viscosity, which is computed for the lithospheric plates and lithologies present in the plate interface (i.e., sediments, basaltic oceanic crust, eclogites, and serpentinies), is defined as $\eta_{yield} = \sigma_{yield}/2\dot{\varepsilon}$, where σ_{yield} is the yield stress as defined by the 2-D Drucker-Prager yielding criterion (Drucker & Prager, 1952; Glerum et al., 2018):

$$\sigma_{yield} = C\cos\phi + P\sin\phi \tag{9}$$

where C is the cohesion and ϕ is the angle of internal friction. The friction coefficient is then $\mu = \sin(\phi)$. We use cohesion values obtained from rock deformation laboratory experiments and friction coefficient estimates consistent with those derived from matching forearc heat flow observations with forward models containing frictional heating along the plate interface (Gao & Wang, 2014). The sediments, basalts, eclogites, and serpentinites have $\phi = 7.47°$ (to reproduce $\mu = 0.13$, after Gao & Wang, 2014) and $C = 5$ MPa (den Hartog & Spiers, 2013), while for the lithospheric plates $\phi = 15°$ and $C = 10$ MPa.The relatively lower plastic strength of the eclogitized layer serves as a proxy for fluid-induced weakening during dehydration (e.g., Hacker et al., 2003). This parameterization ensures that deformation remains localized within the plate interface rather than within the rigid overriding plate. While $\mu = 0.13$ lies near the upper end of experimentally and observationally inferred effective fault friction values, estimates of average shear stress along natural subduction interfaces vary widely depending on geologic setting, inference method, and timescale, with inferred values commonly spanning 10–100 MPa (Behr & Platt, 2013; Duarte et al., 2015; Koyama et al., 2024; Lamb, 2006; Neuharth et al., 2026; Schmidt & Platt, 2022; Von Herzen et al., 2001). Natural subduction interfaces are spatially and temporally heterogeneous and are therefore unlikely to be represented by a single yield stress. We therefore explore a range of interface strengths spanning both weaker and stronger end-member cases.

The initial weak zone, which decouples the plates during subduction initiation, has a viscosity of 2 $\times$ 10^{20} Pa s and a density of 3500 kg/m^3. Within the subducting plate, we assign a quartz rheology to the sediments using the dislocation creep flow law by Tokle et al. (2019). Underneath the sedimentary layer, the basalts are modeled through dislocation creep of Maryland diabase by Mackwell et al. (1998). We implement an irreversible phase transition for the basaltic oceanic crust, which undergoes eclogitization at reference conditions of 1.5 GPa/450°C with a Clapeyron slope $\Gamma = -20 \times 10^6$ Pa/K (e.g., Hacker et al., 2003) to extend this reaction to higher/lower pressures. This phase transition is implemented as an instantaneous densification and switch in the rheological parameters from basalt to Jin et al. (2001)'s eclogite dislocation creep flow law.

This relatively idealized, yet multi-layered, structure–consistent with the inferred structure of oceanic crust (e.g., Schubert et al., 1976)–allows us to test the response of rheologically distinct lithological layers to changes in

velocity and to model the structure and exhumation mechanics within the plate interface (cf. Burov et al., 2001; Ruh et al., 2015; Vaughan-Hammon et al., 2022). In addition to this reference, we examine models with variable interface strengths (i.e., lower/higher friction coefficients for sediments, basaltic oceanic crust, and eclogites) to account for variability in bulk plate interface strength from one margin to another (e.g., Abila et al., 2025). Specifically, we parameterize a weak interface case by choosing, for the listed lithologies, a coefficient of friction $\mu_{weak} = 0.05$ and a strong interface case with $\mu_{strong} = 0.2$; the corresponding value within the reference model is 0.13. These values are within Gao and Wang's (2014) range of estimates for global subduction zones.

We also test the effect of a serpentinite layer underneath the oceanic crust, as this has been demonstrated to facilitate the detachment of oceanic crustal rocks from the slab top within oceanic subduction models, and thereby enhance exhumation and underplating (after Angiboust et al., 2012; Ruh et al., 2015). The serpentinites have an antigorite dislocation creep flow law (Hilairet et al., 2007), and are initiated either as a uniform, 1 km thick layer at the Moho, or as discontinuous lenses with lengths of 84 km and maximum heights of 5 km (Figures S2b and S2c in Supporting Information S1), with reference density of 2700 kg/m^3. These two end-members for serpentinite geometry are inspired by field observations of the structure of the deep oceanic crust at the Southwest Indian ridge (uniform: Muller et al., 1997) and Mid-Atlantic ridge (discontinuous: Cannat et al., 1995), and evidence of discontinuous serpentinization in the rock record (e.g., Pognante et al., 1985). This choice in serpentinite thickness and geometry, albeit larger than the estimates for fast-spreading lithosphere (~500 m; e.g., Pagé & Hattori, 2019), serves as a first-order proxy for the hydrated upper mantle in more mature plates, where deep hydration is facilitated by bending-related faulting at the outer rise (e.g., Ranero et al., 2003). All mechanical and rheological parameters can be found in Tables 1 and 2.

2.4. Mechanical Boundary Conditions

The plate-velocities imposed onto the kinematically driven model are extracted from a dynamic model with similar characteristics as the kinematically driven ones, in order to maintain a slab evolution within our models that is consistent with both our own fully dynamic reference cases and with the general behavior observed in previous dynamic subduction models (Enns et al., 2005; Holt et al., 2015); an overview of the dynamic model is given in Section 2.5. The right boundary is vertically partitioned: at depths shallower than 100 km, we impose inflow rates corresponding to the overriding plate velocity, whereas at depths greater than 100 km, a free-slip condition is applied. Inflow is also applied to the top 100 km of the left boundary, in this case with the subducting plate velocity. Below the lithosphere at the left boundary, this imposed inflow linearly decreases to 0 cm/yr at 200 km. Below this, an open boundary is used wherein material flow can flow inwards or outwards to balance mass within the model, which occurs as a function of pressure departure from the initial lithostatic pressure profile. The upper boundary condition is free surface (Grima & Becker, 2024) and the base is free slip.

2.5. Plate Velocities

The time-dependent plate velocity structure is extracted from a dynamic model that is similar to our kinematically driven models. The two models share the same domain size, plate geometries, and plate ages, but differ in how plate motion is driven. In the dynamic model (Figure S1 in Supporting Information S1), we do not impose plate velocities; instead, both plates evolve self-consistently under buoyancy forces. The lateral boundaries are entirely free-slip; that is, no velocities are prescribed within the lithospheric plates. Another key difference is that, in the dynamic model, the plate interface region is simplified as a 10 km thick layer of isoviscous material; that is, in contrast to the layered lithologies incorporated into the kinematically driven models.

In this dynamic model, the convergence rate increases during the initial, ~13 Myrs-long "free sinking" phase of the model. After which, the convergence rate decreases as the slab tip arrives at the upper-lower mantle boundary, from ~13 to ~17 Myrs, and then proceeds at a near-constant rate until the ~35 Myrs end of the dynamic model (Figure 1b). We call the slowdown event the "dynamic slowdown" and impose this entire velocity evolution on our kinematically driven models. From 35 to 50 Myr, we either impose a ~2.5 cm/yr steady state convergence rate to our kinematically driven models, or apply an additional slowdown in the form of a linear velocity reduction. When applied, we label this second slowdown event a "kinematic slowdown," as this does not arise from the dynamic model, but instead represents externally driven reductions in convergence rate, such as those associated with regional tectonic reorganizations or the subduction of buoyant features (e.g., ridges or seamounts) that may temporarily impede plate motion (e.g., Martinod et al., 2005; Royden & Husson, 2009). We impose 40% of the

Table 2
List of Rheological Parameters With Values and Unit

Parameter	Symbol	Value	Unit
Diffusion creep and dislocation creep			
Prefactors	A_{diff}	Upper mantle diffusion: 1.2×10^{-11}	$Pa^{-1}\ s^{-1}$
		Lower mantle diffusion: 6.3×10^{-14}	$Pa^{-1}\ s^{-1}$
	A_{disl}	Upper mantle dislocation: 1.13×10^{-18}	$Pa^{-n}\ s^{-1}$
		Strong core dislocation: 1.13×10^{-18}	$Pa^{-n}\ s^{-1}$
		Overriding lithosphere dislocation: 1.13×10^{-18}	$Pa^{-n}\ s^{-1}$
		Basalt dislocation: 6.22×10^{-8}	$Pa^{-n}\ s^{-1}$
		Sediments dislocation: 6.54×10^{-31}	$Pa^{-n}\ s^{-1}$
		Eclogite dislocation: 8.84×10^{-11}	$Pa^{-n}\ s^{-1}$
		Serpentinite dislocation: 8.84×10^{-11}	$Pa^{-n}\ s^{-1}$
Exponent	n	Mantle dislocation: 3.5[a]	–
		Strong core: 3.5	–
		Overriding lithosphere: 3.5	–
		Basalt: 4.7[b]	–
		Sediments: 4[c]	–
		Eclogite: 3.4[d]	–
		Serpentinite: 3.8[e]	–
Activation volumes	$V_{a,diff}$	Upper mantle diffusion: 4×10^{-6}[a]	m^3
		Lower mantle diffusion: 2.5×10^{-6}[a]	$m^3\ mol^{-1}$
	$V_{a,disl}$	Upper mantle dislocation: 12×10^{-6}[a]	$m^3\ mol^{-1}$
		Strong core: 2.5×10^{-6}	$m^3\ mol^{-1}$
		Overriding lithosphere: 2.5×10^{-6}	$m^3\ mol^{-1}$
		Basalt: 0[b]	$m^3\ mol^{-1}$
		Sediments: 0[c]	$m^3\ mol^{-1}$
		Eclogite: 0[d]	$m^3\ mol^{-1}$
		Serpentinite: 3.2×10^{-6}[e]	$m^3\ mol^{-1}$
Activation energies	$E_{a,diff}$	Mantle diffusion: 300×10^3[a]	$J\ mol^{-1}$
	$E_{a,disl}$	Mantle dislocation: 540×10^3[a]	$J\ mol^{-1}$
		Strong core: 300×10^3	$J\ mol^{-1}$
		Overriding lithosphere: 300×10^3	$J\ mol^{-1}$
		Basalt: 485×10^3[b]	$J\ mol^{-1}$
		Sediments: 125×10^3[c]	$J\ mol^{-1}$
		Eclogite: 480×10^3[d]	$J\ mol^{-1}$
		Serpentinite: 16×10^3[e]	$mol^{-1}J$
Gas constant	R	8.3145	$J\ mol^{-1}\ K^{-1}$
Pseudo-plastic yielding			
Friction coefficient	μ	0.13[f]	–
Cohesion	C	5[g]	MPa
Angle of internal friction	ϕ	7.47	–

[a]Hirth and Kohlstedt (2003). [b]Mackwell et al. (1998). [c]Tokle et al. (2019). [d]Jin et al. (2001). [e]Hilairet et al. (2007). [f]Gao and Wang (2014). [g]den Hartog and Spiers (2013). From this table we have omitted the rheological parameters for the continental crust and the weak zone, both of which are isoviscous.

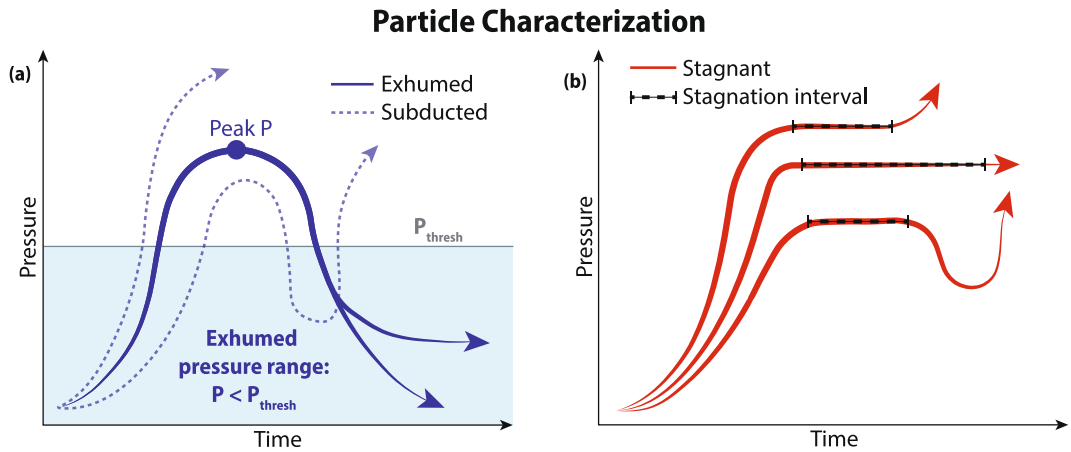

Figure 2. Particle classification within the models: (a) Exhumed particles' pressure-time paths, with their peak pressure; (b) Stagnant particles' pressure-time paths, with graphical representation of the stagnation intervals. The blue area represents the pressure conditions within which a particle needs to remain in order to be considered as exhumed.

convergence rate magnitude to the overriding plate and 60% on the subducting plate; this is both consistent with the ratio of the dynamically modeled subducting plate velocity relative to that of the overriding plate, which has a mean value of ∼1.4, and within the range of average subducting-to-overriding plate velocity ratios in most absolute reference frames (Faccenna et al., 2007; Schellart et al., 2011).

2.6. Particle Characterization

In each model we track ∼50,000 subducting particles (∼60,000 for the serpentinite models, as we track an extra composition). We classify each particle as exhumed, stagnant, or subducted based on their pressure evolution through time and their final position with respect to a set pressure threshold (Figure 2). A particle is considered exhumed if, after reaching peak pressure conditions, its pressure is subsequently reduced by at least 35% of its maximum pressure (P_{thresh}) and remains below this pressure threshold for the rest of the model run (Figure 2). A particle that only temporarily reaches this threshold but later returns to $P > P_{thresh}$ will be classified as stagnant or subducted, depending on its evolution.

A particle is labeled as stagnant if it is not exhumed (following the criteria above) and its pressure remains near-constant for at least 10 Myr, at least once throughout the model run (Figure 2b). A single stagnant particle can have multiple stagnation periods, defined by distinct >10 Myr periods of near-constant pressure. If a particle falls into neither category, it is labeled as subducted. To identify late-stage stagnation, all models are run to 60 Myr. However, only exhumation or stagnation events that initiate before 50 Myr are recorded in our analysis. This cutoff ensures all particles have sufficient time to meet the full exhumation or stagnation criteria by 50 Myr.

Using a non-zero pressure threshold to consider the particles as exhumed is widely used within subduction modeling literature (e.g., Kerswell et al., 2023; Roda et al., 2012; Vaughan-Hammon et al., 2022; Warren et al., 2008). Here, we choose a threshold corresponding to depths well below the surface (i.e., particles remaining at high pressure) to flag particles as exhumed because our models do not contain processes such as erosion, overriding plate extension, or collision, which aid in the final stages of exhumed rock recovery to the surface. Exhumed particles in this study are therefore most comparable to rocks undergoing early-stage exhumation, during which the rocks rise from peak depths but remain sequestered at mid-crustal or upper-mantle depths. Stagnant particles, in turn, only track basal accretion and underplating in the accretionary prism and subduction channel, respectively.

2.7. Numerical Methods

The ASPECT finite element code includes adaptive mesh refinement (AMR), which enables us to achieve very high model resolution in the evolving plate interface region, while limiting resolution in regions with minimal deformation. To achieve this, AMR is applied to model cells with high gradients in viscosity and/or high values of composition (i.e., within the crustal, plate interface lithologies). We also use an ASPECT plugin that sets a

minimum model resolution in the area around the trench. This resolution in this area, which is a box of dimensions (x, y) = (300, 100) km, is set to produce square finite elements/grid cells that are at least 2 km wide/high. The AMR is used to further refine the sediments, basalt and eclogites beyond this resolution. This results in 500 m finite elements along the interface and 12.5 km elements in the lowest resolution regions. In addition, we set the resolution of the upper/lower mantle boundary and the top 100 km of the model to have a minimum finite element size of 3 km, ensuring that all regions of the lithosphere and slab-lower mantle interactions are adequately resolved.

3. Results

3.1. Reference Model

In the reference model, the imposed plate velocities include a single dynamic slowdown event, followed by 30 Myr of near-constant convergence velocities with $v_c \simeq 2.5$ cm/yr (Figure 1) with no additional imposed slowdowns. The resulting evolution of the plate interface is shown for composition, strain rate, and viscosity in Figure 3 in three snapshots corresponding to three different phases of subduction: *(i) subduction infancy* (0.5 Myr), in which the slab begins to sink in the upper mantle and the plate interface evolves from its initial configuration, *(ii) dynamic steady state* (25 Myr), achieved after the dynamic slowdown event, during which the plate interface experiences a rearrangement of its internal structure in response to the previous plate velocity reduction, and *(iii) kinematic steady state* (45 Myr), where the imposed velocity is constant and equal to the velocity attained at the end of phase *ii*.

During the early stages of subduction a décollement develops within the oceanic crust (~500 m below the slab surface), enabling the subsequent downdragging of incoming sediments into this zone (Figure 3a, Movie S1). As the sediments are weak, their emplacement in the interface triggers a migration of the main shear zone from the top of the stronger oceanic crust to the base of this sediment layer (Figures 3b and 3c). This localization promotes the detachment of slivers of the overlying intruded sediment, along with adjacent portions of the basaltic crust and eclogites, and their subsequent exhumation and/or accretion to the overriding plate (Movie S1).

As a result, two levels of exhumation and stagnation emerge: (a) the shallow accretionary prism (to ~40 km depth) that is mostly composed of sediments intercalated with fragments of oceanic crust, and (b) the deeper subduction channel (extending to ~100 km), along which more distributed slicing of oceanic crust occurs. We compare the distribution of peak pressure-temperature (P–T) conditions of the modeled subducted, exhumed and stagnant particles to Agard et al.'s (2018) compilation of the peak P–T conditions recorded by metamorphic rocks exhumed within accretionary complexes representing paleo-oceanic subduction (Figure 4). Full P–T and P-t paths are shown in Figure S3 in Supporting Information S1, and representative exhumation rates and P–T–t paths for exhumed particles in Figure S4 in Supporting Information S1. We omit the P–T conditions of metamorphic soles from this database, as we initially prescribe the slab to 75 km depth and so cannot reproduce the relevant subduction initiation conditions. We also indicate the percentage of exhumed and stagnant particles relative to the entire subducting crust and sediments. The P–T conditions of modeled exhumed and stagnant particles are significantly colder than temperatures estimated from the rock record, as also observed in previous studies (Agard et al., 2018; Penniston-Dorland et al., 2015). At equivalent pressures, exhumed particles are slightly cooler than stagnant ones (Figure 4b). This is due to the evolving slab thermal conditions during time-dependent subduction evolution (e.g., Holt & Condit, 2021; Turino & Holt, 2024): While stagnation occurs throughout the model, all exhumed particles reach peak pressure during the fast "free sinking" phase during which the slab is coldest (Figure S5 in Supporting Information S1).

Overall, exhumed particles (Figure 4b, circled in black) comprise 3.7% of subducted crust (Figure 4c), and record relatively low pressure (up to ~1 GPa) and low temperature (<200°C) conditions. All exhumed particles are either sediments or basalts, with the sediments dominating (3.5% of all tracked particles and 20% of subducted sediments, vs. 0.2% of tracked particles and 0.3% of subducted oceanic crust). Stagnant particles correspond to 17.9% of all tracked particles (Figure 4c) and have maximum P–T conditions of 2.5 GPa/450°C. Among these, sediments dominate (11.1% of all tracked particles and 65% of subducted sediments), with more minor contributions from basalts and eclogites.

Exhumation and stagnation are tightly linked to the imposed plate velocity, which evolves through three main phases. During the first, slow phase at the onset of subduction, a primary shear zone forms within the weak

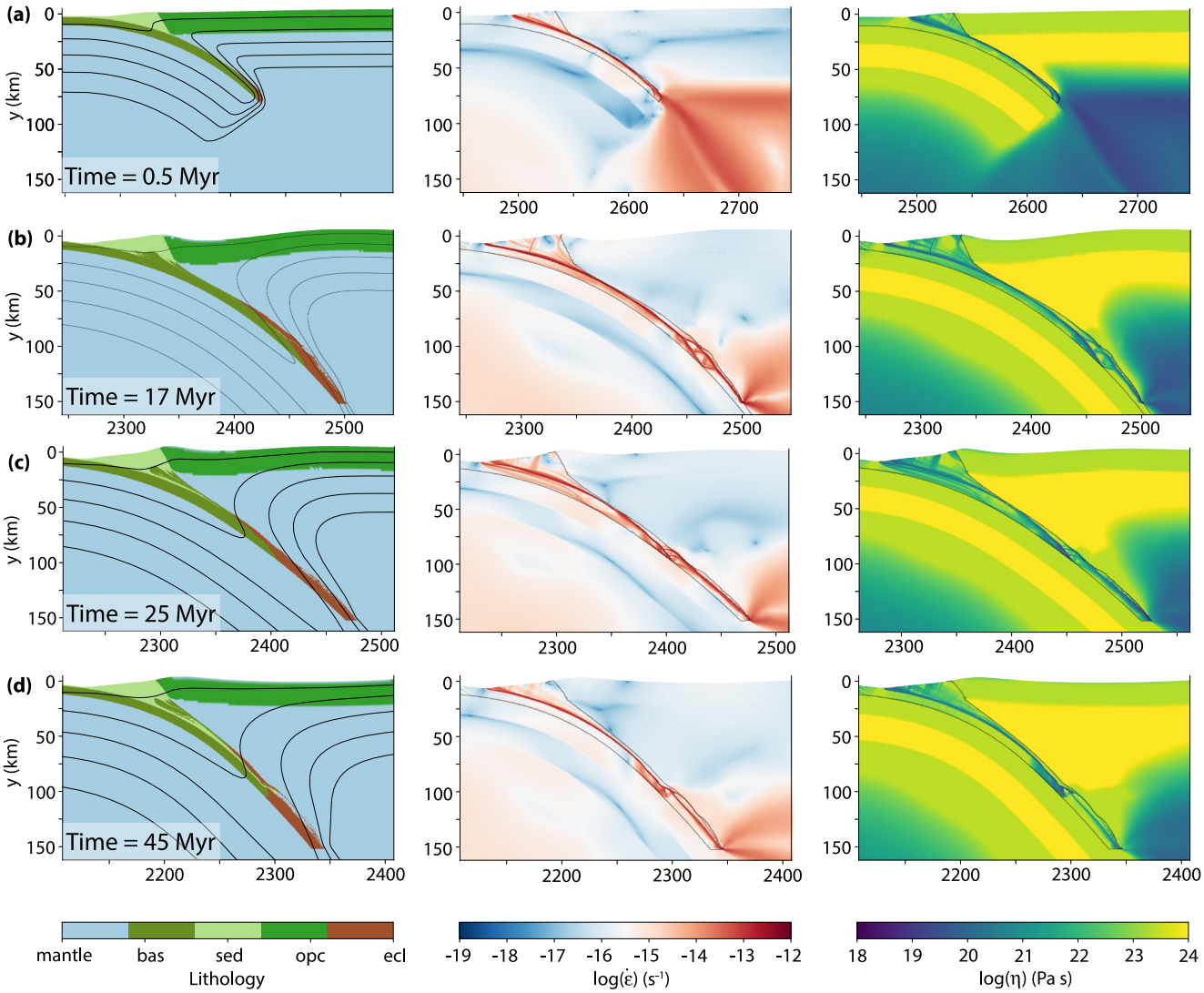

Figure 3. Evolution of the plate interface in the reference model at (a) 0.5 Myr (subduction infancy), (b) 17 Myr (exhumation onset), (c) 25 Myr (dynamic steady-state), and (d) 45 Myr (kinematic steady-state), shown through the main lithological compositions, strain rate, and viscosity. The black contours correspond to isotherms at 100, 300, 500, 700, 900°C. The strain rate and viscosity plots depict a distinct main shear zone migrating from the top of the oceanic crust to the base of the sediment layer. The gray contour corresponds to the outline of all the lithologies of interest for exhumation and stagnation processes (sediments, basaltic oceanic crust, and eclogites).

oceanic crust (~500 m below the slab surface; Figure 3b). This shear zone remains active throughout the model run, acting as a long-lived area of weakness and a conduit for sediment emplacement into the plate interface. During this early stage—before the onset of free sinking—sediments are emplaced along this shear zone, locally detaching small slivers of oceanic crust at shallow (≤50 km) depths (Figure 5b). Exhumation and stagnation of these shallow slivers, however, does not take place during this early stage, as the free-sinking phase initiates soon after, at 7 Myr into the model run.

During this free-sinking phase, the subduction velocity increases sharply. With a high subduction velocity, the interface is carried downward as a coherent part of the slab, and thus no exhumation or stagnation of the above-mentioned shallow slivers occurs during this stage. This rise in subduction velocity also inhibits new sediment subduction: incoming, weak sediments are largely decoupled from the slab and accumulate in the shallow accretionary prism (Figure S6 in Supporting Information S1). The sediments emplaced in the interface during the prior, slow subduction phase are rapidly dragged at depth with the slab along the main shear zone, inducing slicing of oceanic crust and eclogites along the deep interface.

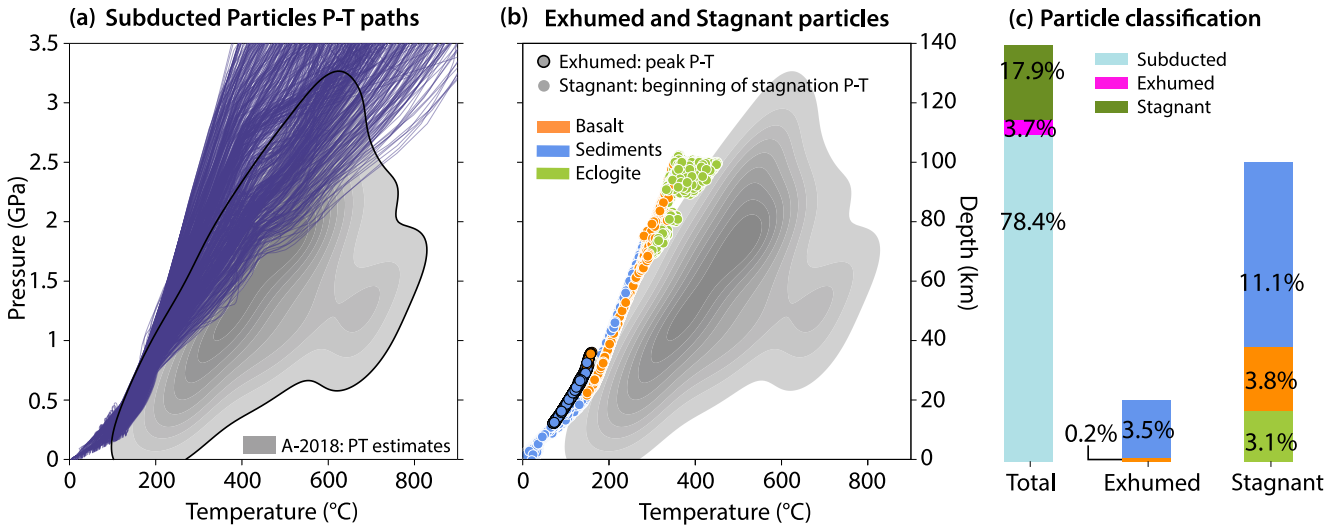

Figure 4. (a) *P–T* paths for subducted particles, plotted against a smoothed density estimate of the Agard et al. (2018) database (grey shading), generated using kernel density estimation; metamorphic soles are excluded. (b) Peak *P–T* conditions for exhumed particles and the *P–T* conditions of stagnating particles at the onset of stagnation, grouped by lithology and compared to rock record *P–T* estimates. (c) Percentages of subducted, exhumed, and stagnant particles, including a breakdown of exhumed versus stagnant lithologies and their associated volumes.

As the slab approaches the lower mantle, the velocity of subduction rapidly decreases. This third phase of subduction, the "dynamic slowdown," correlates with the renewed and steady emplacement of sediments along the pre-existing main shear zone. Continuous sediment emplacement in the plate produces the final slicing of sediments, oceanic crust and eclogites along the whole interface, leading to the complete decoupling between the interface itself and the underlying subducting slab. Detached material deforms during the slowdown, and the main slice of detached slab material to splits into further fragments into smaller slivers at shallow depths, as strain localizes along the pre-existing main shear zone (Figure 3; Figure S6 in Supporting Information S1). During this prolonged period of low convergence rate, the detached material is now able to exhume and/or stagnate.

Exhumation occurs within the accretionary prism, with slices reaching the exhumation threshold P_{thresh} at different times depending on their lithology, thickness (0.5–2 km), and depth (Figure S7 in Supporting Information S1). Exhumation velocities peak at ∼2 mm/yr (Figure S4 in Supporting Information S1), consistent with estimates for active accretionary wedges (1–10 mm/yr) from low–temperature thermochronology and microstructural strain rate analysis of mylonitic shear zones in active complexes such as the Olympic mountains (Angiboust et al., 2022). Sediments, being more buoyant, are exhumed first, followed by oceanic crustal slices, producing the clustered temporal distribution shown in Figure 6. Along the deeper interface, up to ∼100 km depth, the arrival of sediments along the main shear zone drives progressive detachment of slices of sediments, basalts, and eclogites. This punctuated detachment continues from the onset of dynamic slowdown until the end of the simulation, producing particles that stagnate at near-constant depths but do not exhume. We observe a clustered distribution for the onset time of stagnation (Figures 5c), and a minimum average stagnation duration of ∼15 Myr. Lithology-specific minimum stagnation durations are 23 Myr for sediments, 12 Myr for eclogites, and intermediate values for basalts (Figure 5d).

3.2. Plate Velocity Comparison

To further isolate the effect of plate velocity changes on exhumation and stagnation, we run two models with a second "kinematic slowdown" event 20 Myr after the dynamic slowdown (i.e., 35 Myr from the start of the model). We test the effect of a linear reduction from the steady-state velocity $v_c \simeq 2.5$ cm/yr to 50% ("50% velocity" model) or 0% ("0% velocity" model) of this value, and compare the timeline of exhumation and stagnation to the results described in the previous section. After 45 Myr, the channel exhibits a similar lithological structure regardless of the velocity slowdown, while the plate interface strain rate decreases as the velocity is reduced, indicating increased coupling between the plates (Figure 7; Figure S8 in Supporting Information S1). The effect of this channel evolution on exhumation and stagnation is shown in Figure 7.

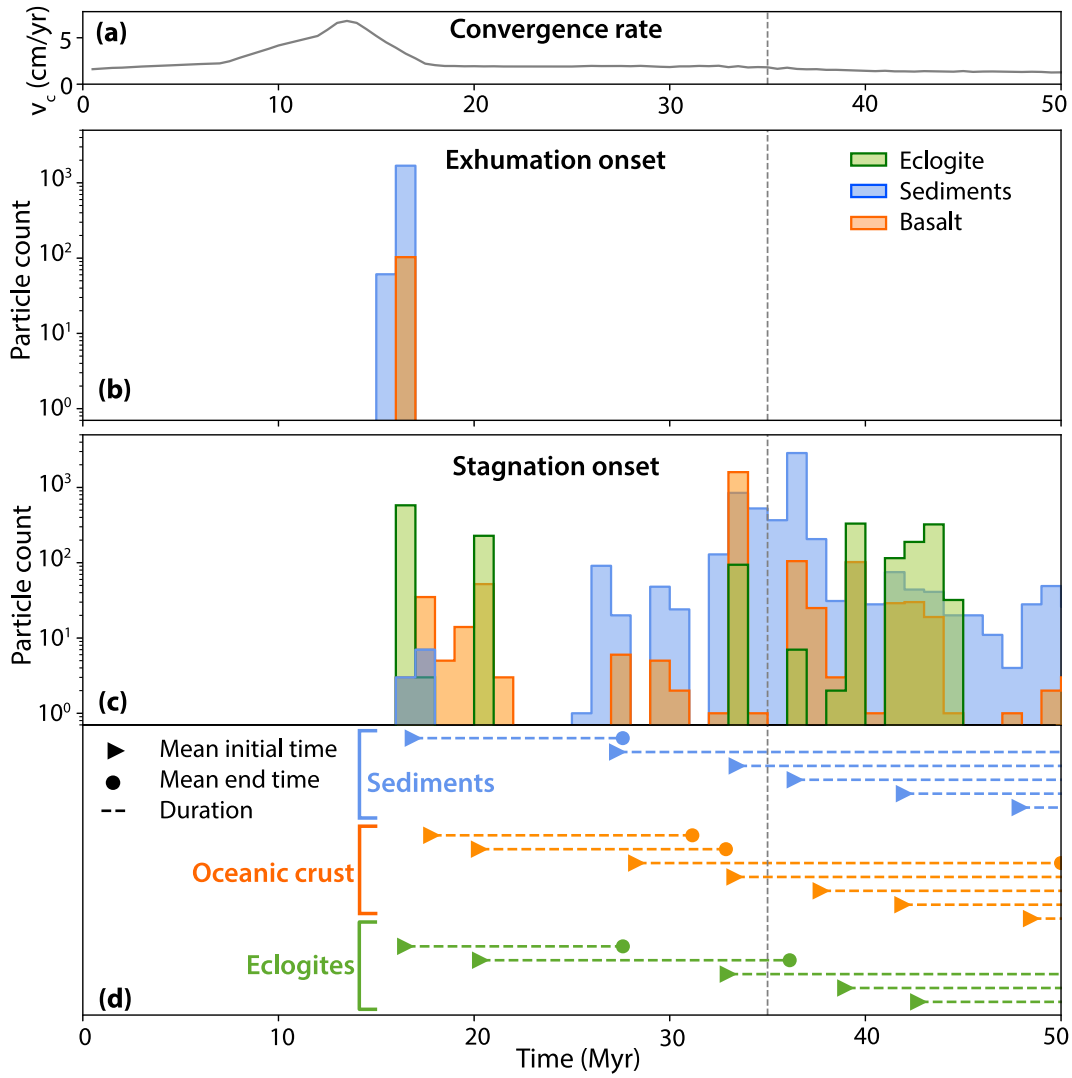

Figure 5. Timeline of exhumation and stagnation versus convergence rate. (a) Convergence rate for the reference model. (b) Time at the onset of exhumation, by lithology, versus particle count (log scale). (c) Time at the beginning of stagnation, by lithology, versus particle count. (d) Mean stagnation intervals for particles in (c), binned by stagnation onset in 5 Myr intervals; each line corresponds to the mean start, end, and duration for one lithology within a single 5 Myr bin.

For all cases, as plate velocity is reduced, the volume of exhumed particles decreases (Figures 7d, 7g, and 7j), from 3.7% of tracked particles in 100% velocity case, to 3.6% in the 50% velocity case, and 2.4% in the complete-slowdown model. The temporal distribution also changes: as the late-stage plate velocity decreases, the volume of particles exhumed during the dynamic slowdown phase decreases, with no basalt exhumation in the 0% velocity case (Figures 7b, 7e, and 7h). This is due to the drastic reduction in traction at the base of the accretionary prism, as the velocity decreases, which results in the progressive weakening and eventual cessation of corner flow in the zero-velocity model. With corner flow weakened, the slab drags a portion of the otherwise exhumed particles (i.e., in the reference case) to depth during the late subduction phase (Figure S9 in Supporting Information S1). The plate interface strain rate (Figure 7), in this model, decreases by almost two orders of magnitude at the base of the prism, illustrating this increased coupling.

Conversely, the volume of stagnating particles increases as late-stage plate velocity is decreased, from 17.9% of tracked particles in the reference model, to 19.5% and 22.6% in the 50% and complete slowdown cases, respectively (Figures 7d, 7g, and 7j). This complex behavior is due to different processes within the different levels of the plate interface: at shallow depths in the prism (≤40 km), the reduction of corner flow in models with

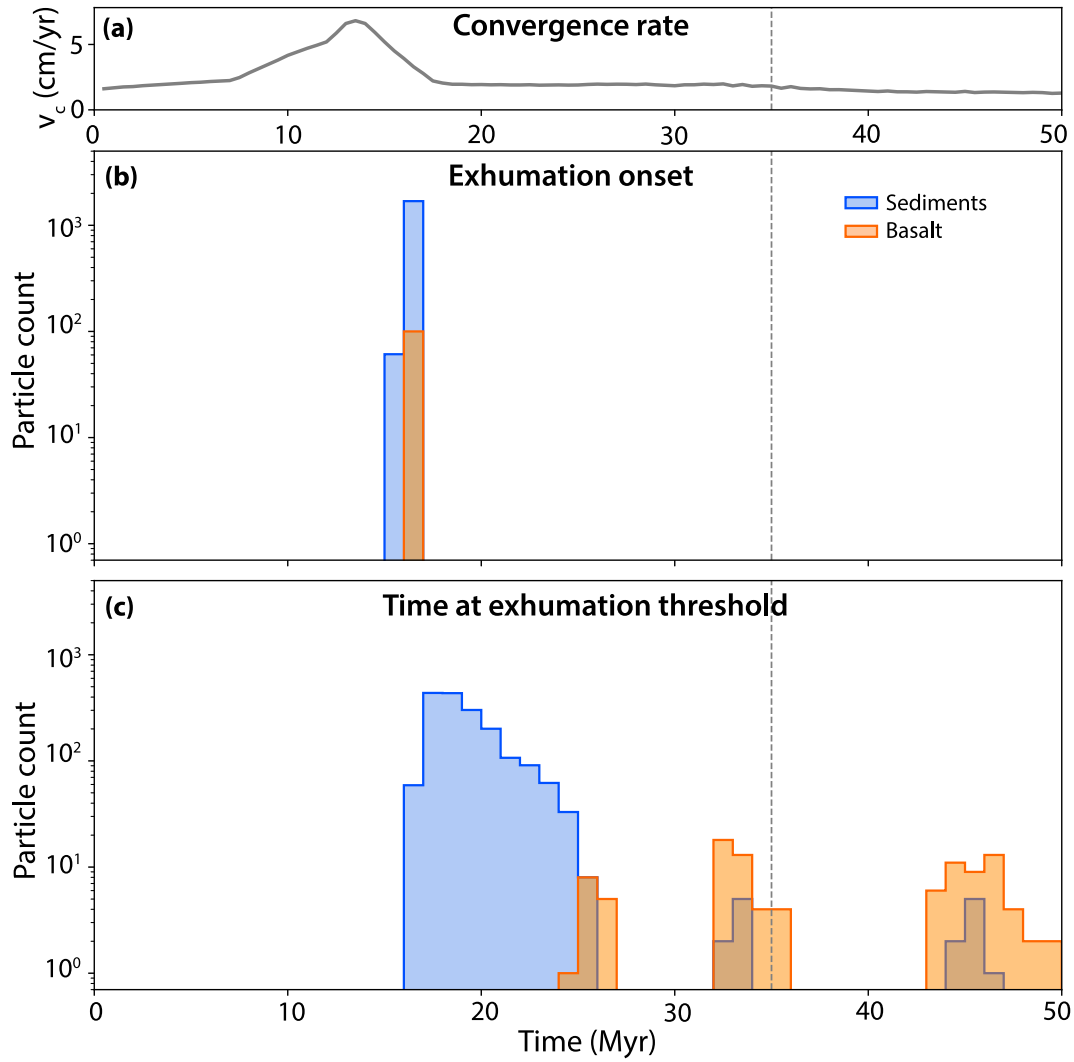

Figure 6. Timeline of exhumation against convergence rate. (a) Convergence rate for the reference model. (b) Time at the onset of exhumation, by lithology, versus particle count (log scale). (c) Time at which the particles reach the exhumation threshold, by lithology, versus particle count.

lower late-stage plate velocities results in late subduction of particles that have previously risen past the exhumation threshold. Some of these particles eventually stagnate in the accretionary prism, hence registering as stagnant as opposed to exhumed (Figure 7, Figure S10 in Supporting Information S1). Deeper (≤100 km), the reduction in basal shear stress enables buoyancy forces to balance the down-dragging shear stress for a larger proportion of buoyant particles and hence results in the stagnation of particles that are subducted in the reference.

3.3. Interface Structure and Rheological Tests

We now examine how different rheological parameterizations (low vs. high yield stress) and compositions (addition of basal serpentinite) of the plate interface impact exhumation and stagnation (Figure S2 in Supporting Information S1). The resulting interface shapes and volumes of exhumation and stagnation are shown in Figure 8. Overall, a weaker interface produces a wider and deeper prism with a subduction channel starting below 80 km (Figures 8b–8d), while stronger rheologies produce the distinctive shallow accretionary prism and, as in the reference model, a thin subduction channel below 50 km depth (Figure 8a). As in the reference case, all exhumed particles detach from the slab during one punctuated event that occurs either during or after dynamic slowdown, but the time at which the particles reach the exhumation threshold is dependent on the interface strength, as is the time of stagnation of the particles along the interface (Figures 9 and 10).

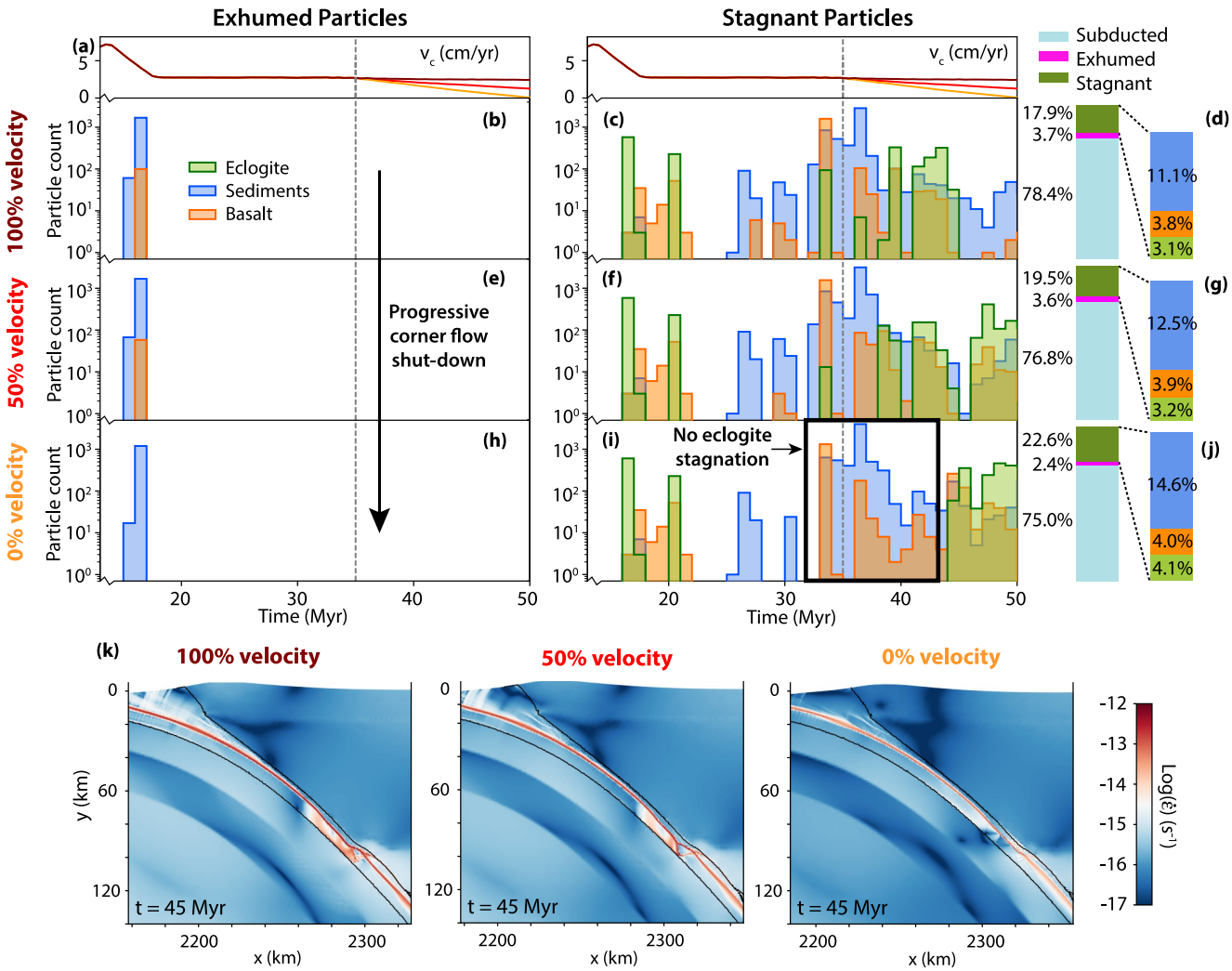

Figure 7. Timeline of exhumation and stagnation against convergence rate. (a) Convergence rates. Time at the onset of exhumation and stagnation, and percentage of subducted, exhumed and stagnant particles (broken down into lithology) respectively, for: (b–d) Reference model (100% velocity), (e–g) 50% velocity model, (h–j) 0% velocity model. (k) Strain rate distribution along the plate interface for these models, showing the progressive reduction in strain rate magnitude of the main shear zone. Note that the *x* axis starts at the time of the peak in convergence rate, identified by the zigzag line at the start of the axis.

3.3.1. Yield Stress

A low yield stress ($\mu = 0.05$, Figure 8a), results in large amounts of shallow exhumation (7.2% of crustal particles; pressures up to 0.8 GPa) and stagnation (26.9%, up to 1.5 GPa; Figure S11a in Supporting Information S1), while a high yield stress ($\mu = 0.2$, Figure 8b), produces much less exhumation (2.1%, up to 1 GPa) and negligible, but deeper stagnation (1.0%, up to 2 GPa; see Figure S11b in Supporting Information S1). In the lower yield stress case, no sediments are subducted beyond ~20 km depth but the crust is weak enough for significant thickening of the interface without localized tectonic slicing. Pervasive corner flow therefore takes place in the weakened accretionary prism (Figure S11a in Supporting Information S1). In the high yield stress case, deep sediment subduction occurs only prior to the free sinking phase, while after dynamic slowdown, sediments are subducted only to shallow levels and contribute to the thickening of the accretionary prism. The inhibition of deep sediment subduction prevents tectonic slicing of basaltic crust/eclogites deeper than 20 km and so only minimal material is exhumed within a mainly sedimentary prism. Although stagnation volumes are negligible within this model, eclogite facies conditions are reached due to a single burst of sediment emplacement in the deep channel early in the model run (Figure S11b in Supporting Information S1).

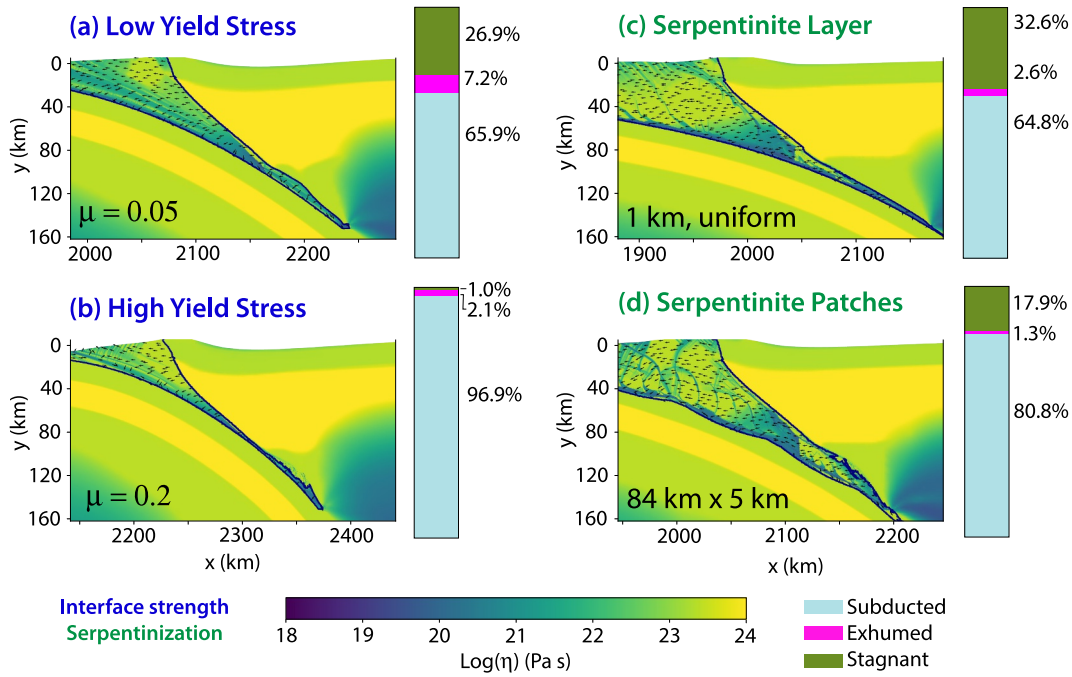

Figure 8. Interface shape, strength and percentage of subducted, exhumed and stagnant particles for different rheological properties, divided by interface strength (dark blue) and serpentinization (green). The arrows (black) indicate the flow direction within the interface (not scaled by magnitude). Velocities external to the interface are not shown. (a) Low and (b) high yield stress; A weak interface is also modeled through the presence of a weak layer of serpentinites under the oceanic crust, either as (c) a uniform, 1 km thick layer or (d) serpentinite patches long 84 km with maximum thickness 5 km.

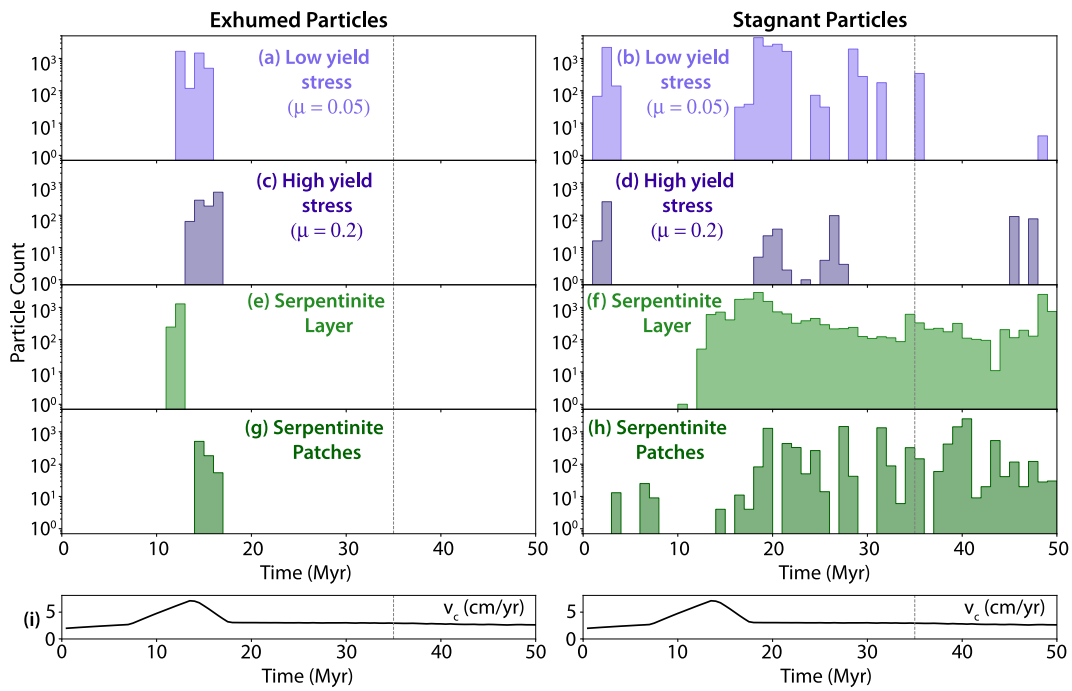

Figure 9. Timeline of exhumation (left panels) and stagnation (right panels) against convergence rate (i) for: (a–b) low yield stress, (c–d) high yield stress, (e–f) serpentinite layer, (g–h) serpentinite patches.

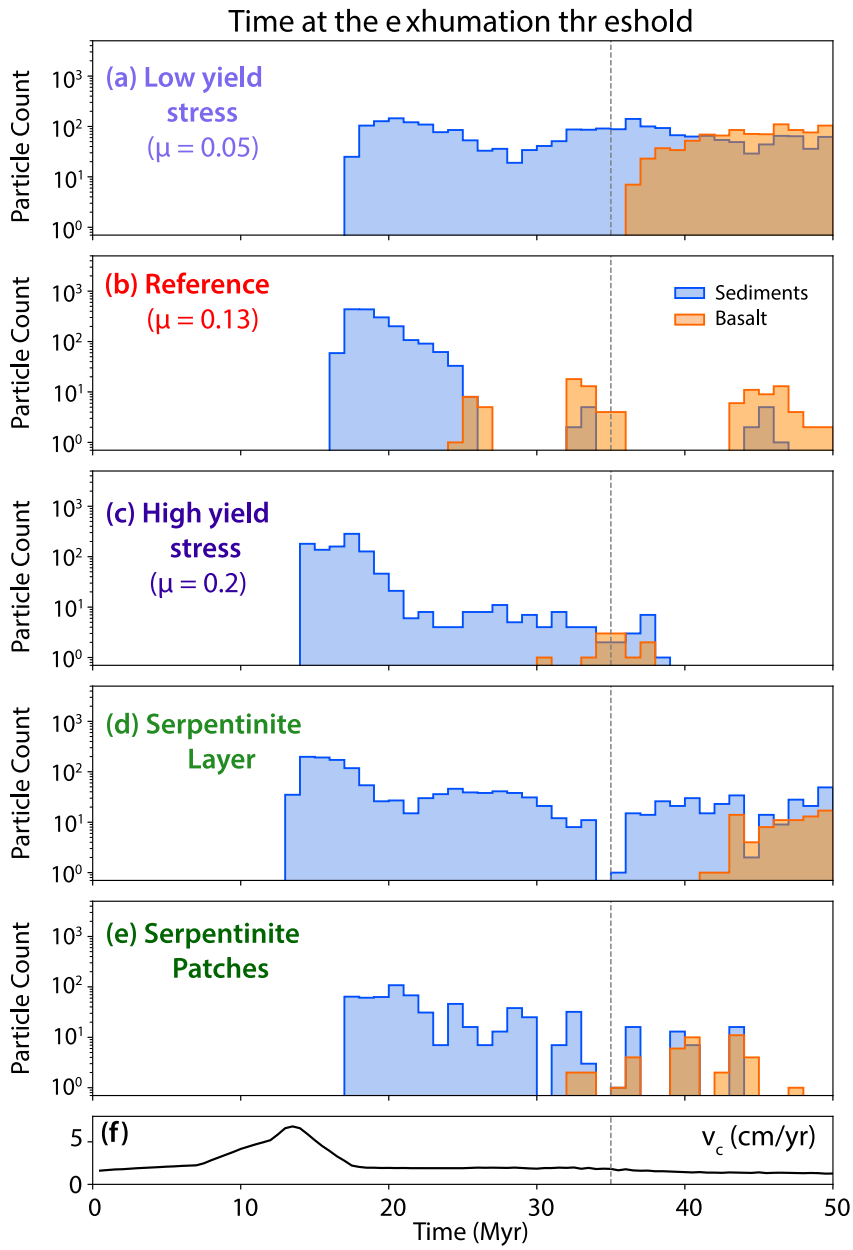

Figure 10. Time at the exhumation threshold against convergence rate (f) for: (a) low yield stress, (b) reference model (moderate yield stress), (c) high yield stress, (d) serpentinite layer, (e) serpentinite patches. The colors in the plot show the lithology of the exhumed particles, where blue identifies sediments and orange the basaltic oceanic crust.

Although all exhumed particles detach from the slab at the onset of dynamic slowdown regardless of interface strength, the time at which the exhumed particles reach the exhumation threshold depends strongly on the interface rheology (Figure 10). Exhumation velocities also vary with interface strength, reaching peak values of ~4 mm/yr for $\mu = 0.05$ and ~6 mm/yr for $\mu = 0.2$ (see *P–T-t* paths and burial and exhumation velocities in Figures S12 and S13 in Supporting Information S1). The pervasive corner flow within the deep accretionary prism in the weak model generates continuous and delayed exhumation of basalts from 35 Myr into the model run (Figure 10a). A higher yield stress, conversely, results in one punctuated basalt exhumation event (Figure 10c). This differs from the reference model, in which there are three clusters of particles reaching the exhumation threshold (Figure 6c, Figure S7 in Supporting Information S1). Sediment exhumation is, however, continuous and long-lived in both models (Figure 10). In both cases, stagnation is episodic (Figures 9b and 9d). For low yield

stress, this is mostly sediment stagnation occurring at shallow depths (Figure S11a in Supporting Information S1). In the high yield stress case, this also includes stagnation of warm basalts and newly formed eclogites (Figure S11b in Supporting Information S1).

3.3.2. Serpentinite

We analyzed models with two serpentinite geometries (Figures 8c and 8d): (a) a continuous, 1 km thick layer, and (b) patches, which are 84 km long and have a maximum thickness of 5 km (Figure S2 in Supporting Information S1). In both cases, adding weak serpentinites under the crust localizes strain in this region, decoupling the whole slab crust, and resulting in the formation of a wide and deep prism that can reach depths of 140 km. The interleaving of sediments, serpentinite and basalts/eclogite is enhanced relative to the reference model, impacting both exhumation and stagnation. Both models produce less exhumation than the reference (layer: 3.3% of crustal particles; patches: 1.3%; reference: 3.7%). As the extreme crustal thickening occurs more rapidly than the trench retreats, particles are added to the growing wedge instead of rising toward the surface, and hence preferentially stagnate rather than exhume. This leads to a maximum wedge thickness (up to ∼60 km) that represents a mechanical end-member for systems with continuous, highly efficient décollements; while this exceeds the dimensions of modern accretionary wedges, it serves as a baseline for the impact of extreme crustal decoupling.

In the uniform serpentinite layer case, pervasive and relatively continuous stagnation takes place along the whole prism (32.6% of tracked material), with maximum pressures of 3.5 GPa (Figure S14a in Supporting Information S1). This is because the positive buoyancy of the serpentinites supports, and hence aids, the stagnation of all lithologies, including the dense eclogites. Sediments and basalts dominate (26.7% of total); together serpentinites and eclogites comprise just 5.9% of all the tracked material, roughly half each. Despite their small fraction, the comparable amounts demonstrates that serpentinites aid the detachment of the denser eclogites from the slab top (cf. Angiboust et al., 2012; Ruh et al., 2015). The presence of serpentinite patches, on the contrary, reduces stagnation compared to the uniform layer case (17.9% of tracked lithologies), as their irregular geometry promotes continuous deformation and lateral re-circulation within the prism. However, the simultaneous crustal thickening inhibits excessive vertical motion of all lithologies and so, despite this re-circulation, most particles neither experience a great enough pressure decrease to be considered exhumed, nor are stable enough to be classified as stagnant. As in the layered serpentinite case, stagnation takes place along the whole interface, up to 3.2 GPa (Figure S14b in Supporting Information S1), but, in contrast, both exhumation and stagnation are significantly more episodic (cf. Figures 9f, 9h, 10d, and 10e).

As in all previous models, all exhumed particles detach from the slab at the onset of dynamic slowdown (Figures 9e and 9g). The distribution of times at which the exhumed particles reach the exhumation threshold shows that in both the uniform and patchy serpentinite cases, buoyant sediments are exhumed with peak exhumation velocities of ∼1.5 mm/yr (uniform layer) and up to ∼3 mm/yr (serpentinite patches, with larger variability due to patch geometry), while denser basalts detach deeper and reach the exhumation threshold later with lower peak velocities (Figures 10d and 10e, Figures S15 and S16 in Supporting Information S1).

4. Discussion

In the following sections, we describe how the evolving subduction interface interacts with time-dependent plate velocities and leads to distinct depths of exhumation and stagnation within our models. We then place these results in the context of previous modeling and field studies.

4.1. Plate Interface Structure, Exhumation, and Stagnation Pathways

In agreement with previous subduction modeling studies, we observe exhumation and stagnation at two different levels within our models (Figure 11): the accretionary prism (≤40 km depth; e.g., Allemand & Lardeaux, 1997; Beaumont et al., 1999; Cloos, 1982; Cowan & Silling, 1978; Giunchi & Ricard, 1999; Menant et al., 2019; Van Dinther et al., 2012; Yamato et al., 2007) and the subduction channel (≥40 km depth; e.g., Burov et al., 2001; Gerya et al., 2002; Shreve & Cloos, 1986; Wang et al., 2019; Vaughan-Hammon et al., 2022). The exhumed particles are sourced primarily from the accretionary prism, while stagnation occurs both within the prism and in the deep subduction channel (Figure S17 in Supporting Information S1). These two levels of material transfer and exhumation provide the first-order framework against which we compare our model predictions with natural

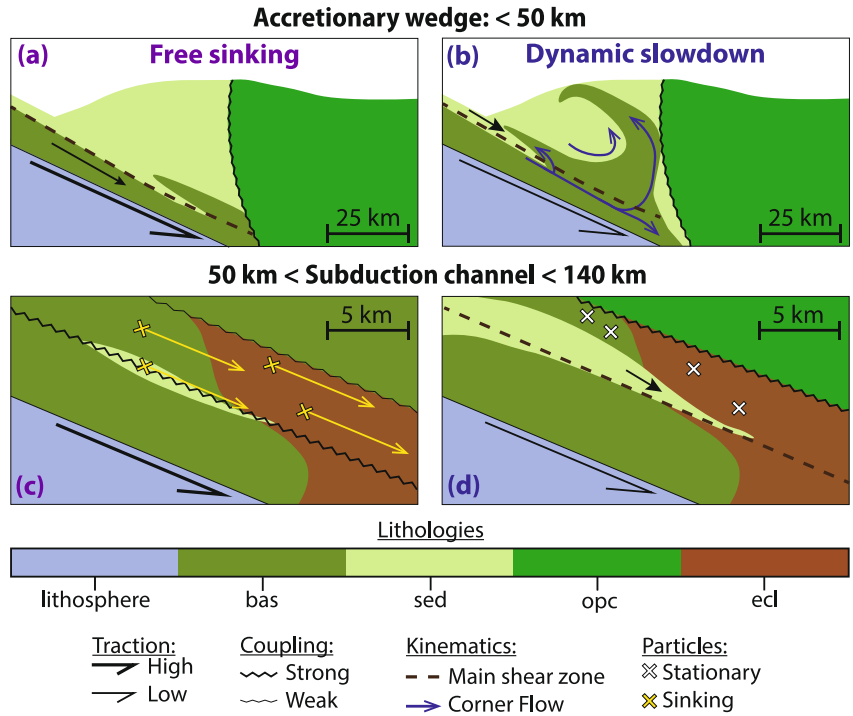

Figure 11. Schematics of the main mechanisms in the accretionary prism and in the deeper subduction channel during free sinking and dynamic slowdown. (a), (c) For the reference case, the fast subduction phase (free sinking) inhibits the subduction of sediments and results in an accretionary-type subduction zone; deeper in the channel, all lithologies are coupled to the sinking slab and subduct coherently (yellow x with arrows). (b), (d) As subduction slows down, sediments can be emplaced in the plate interface along the main shear zone, isolating the plate interface from the sinking slab; exhumation takes place in the accretionary prism through corner flow, and deeper in the interface slices of all lithologies are strongly coupled to the overriding plate and stagnate (white x). In this diagram, the zigzag line represents coupling, with a rougher line indicating stronger coupling, and the main shear zone is indicated by a dotted line.

subduction systems in Section 4.3, where we characterize the depth domains, durations, and material pathways represented by the rock record.

In the accretionary prism, deformation is largely controlled by sediment influx and the induced interface weakening. Most of the exhumed material is sedimentary (up to ~5% of total subducted crust volume), with a lower amount of basaltic oceanic crust (up to ~2.3%). This is compatible with estimates from the global compilation of exhumed metamorphic rocks at oceanic subduction zones, which indicate that less than 5% of oceanic crust is typically exhumed (Agard et al., 2009; Lallemand et al., 2024). In our models, exhumation in the prism takes place as a result of corner flow that mobilizes slices of sedimentary and crustal material detached from the underlying slab (cf. Allemand & Lardeaux, 1997; Cowan & Silling, 1978; Giunchi & Ricard, 1999; Menant et al., 2019; Ruh, 2020; Ruh et al., 2015; Van Dinther et al., 2012; Yamato et al., 2007). These slices detach through down-stepping of the main shear zone within the plate interface, initiated by an early décollement in the oceanic crust and reinforced by subsequent sediment emplacement (Figure 5a, Figure S6 in Supporting Information S1; schematic in Figure 11a). However, while significant volumes of sediment and basalt are exhumed from accretionary prism depths in our models, we do not produce exhumation of deep-seated eclogite-facies rocks from the subduction channel. This may reflect the absence of fluid-related effects, such as enhanced interface weakening (e.g., Angiboust et al., 2012), or may simply arise from model resolution limitations. In the rock record, eclogites commonly occur as blocks ranging from centimeters to hundreds of meters in size embedded within buoyant sediment or serpentinite matrices (e.g., Coleman & Lanphere, 1971; Whitney & Davis, 2006), whereas our models, with a minimum resolution of 500 m, cannot capture such fine-scale mixing and preservation. Conversely, eclogite exhumation could also be primarily associated with the occurrence of major tectonic events, such as extreme slab rollback (e.g., Brun & Faccenna, 2008) or slab break-off (e.g., Chemenda et al., 1995; Duretz et al., 2011, 2012; Ernst et al., 1997), which are also not modeled in this study.

Along the whole plate interface, stagnation of sediments, basalts and eclogite results from the progressive detachment of slivers of slab material and their coupling to the overriding plate (as also evidenced in the rock record, e.g., Reinecke, 1998; Angiboust et al., 2011). In the accretionary prism, stagnation involves only sediments and basaltic oceanic crust, in a process akin to basal accretion (cf. Angiboust et al., 2022; Kukowski et al., 2002; Malavieille, 2010; Menant et al., 2019; Perrin et al., 2013). In the deeper channel, all lithologies stagnate, including eclogites (Figure 4c), which corresponds to underplating within the deep channel (≥60 km; cf. Kotowski et al., 2022; Ruh et al., 2015). Such long-lived stagnation of eclogitic material is consistent with field and geochronological observations suggesting large slivers may remain at depth for several Myr before being exhumed during subsequent tectonic events (Angiboust & Glodny, 2020; Minnaert et al., 2024).

Interface strength strongly controls the geometry and efficiency of exhumation and stagnation. Weak interfaces (low yield stress case; Figure 8a) favor a wide accretionary prism and larger exhumation volumes but limit the pressures reached by stagnant material. Relatively strong interfaces (both the high yield stress and references cases; Figure 8b) reduce prism size yet enable deeper, higher-pressure stagnation, including eclogite-facies conditions. Abyssal serpentinization (Figure 8c) further facilitates deep stagnation, while exhumation remains confined to shallow levels (≤50 km). By both weakening the deep interface and increasing positive buoyancy, serpentinites facilitate deep stagnation of eclogites (up to 140 km and 3.5 GPa; Figure S11 in Supporting Information S1) (Ruh et al., 2015). Menant et al. (2019) identified high shear stress domains along the interface as potential zones of detachment. Our results indicate that the actual occurrence of detachment is further regulated by the plastic yield stress; in cases with lower yield stress, deformation remains diffuse and strain localization is insufficient to produce discrete detachment, leading instead to a thickening of the accretionary wedge. This bolsters inferences from previous modeling studies that the rheology of the interface has a crucial impact on the volume and depth of exhumation (Burov et al., 2001; Gerya et al., 2002; Malatesta et al., 2012; Menant et al., 2019; Vaughan-Hammon et al., 2022; Wang et al., 2019; Yamato et al., 2007).

Building on this groundwork, we provide a systematic characterization of how the lithological and rheological structure of the plate interface sets the stage for various exhumation and stagnation mechanisms that dominate within different levels of the plate interface. As covered in the next section, these mechanisms are not only highly dependent on the rheological parameterization of the plate interface, but also the imposed plate velocity evolution. In this context, the geological record provides key constraints on expected depth distributions, residence times, and exhumation styles, which we summarize in Section 4.3 and use to evaluate model behavior.

4.2. Time-Dependent Model Behavior

The plate interface deforms in response to time-dependent plate velocity through three main phases: (a) subduction infancy and free sinking (≤7 Myr), characterized by increasing convergence rates, (b) dynamic slowdown (13–25 Myr), during which convergence rates sharply decrease, and either (c) a dynamic steady state with $v_c \simeq 2.5$ cm/yr or an imposed kinematic slowdown (35–50 Myr) used to explore the effects of a further velocity reduction to the point of (near) cessation of subduction. These temporally evolving regimes are interpreted in light of first-order constraints from the rock record (Section 4.3), which document characteristic durations and episodic versus continuous behavior of exhumation and underplating in natural subduction zones. Throughout this evolution, the main shear zone reorganizes in response to velocity changes, modulating sediment input and the degree of coupling between the slab and the interface. During early subduction, initial sediment slices are emplaced along the interface, locally slicing the oceanic crust. However, exhumation is inhibited during the free-sinking phase, when the interface is carried downward coherently with the slab and the accretionary prism remains mechanically decoupled. When convergence rates decrease during dynamic slowdown, renewed sediment influx into the pre-existing shear zone promotes further slicing of sediments, basalts, and eclogites along the interface (Figure 11). Unlike earlier slices, these late-stage slices are no longer entrained by a rapidly sinking slab and can therefore stagnate or exhume, consistent with basal accretion and transient deep slicing observed in previous numerical studies (e.g., Ellis et al., 1999; Menant et al., 2019; Ruh, 2020; Ruh et al., 2015). This transition marks the shift from a short-lived slicing regime to a longer-lived mode that persists into steady-state subduction.

The resulting deformation style depends strongly on interface strength. Strong interfaces promote efficient strain localization along discrete shear zones at lithological boundaries within subducted sediments or at the top of the oceanic crust (Figures 3 and 8), consistent with field observations that exhumation is favored along lithological boundaries (e.g., Angiboust et al., 2011; Hermann et al., 2000; Laurent et al., 2016; Philippot & van

Roermund, 1992; Smye & England, 2023). In contrast, weaker interfaces suppress localization, leading to more distributed shear, thickening of the accretionary prism, and reduced sediment subduction, as commonly documented in modeling studies (Duarte et al., 2015; Tan et al., 2012; Tulley et al., 2020). Despite these rheological differences, exhumed particles consistently detach near or shortly after the dynamic slowdown event (Figure 11). This suggests that exhumation is significantly triggered by changes in plate velocity, although factors such as interface strength and slab composition provide important secondary controls. Interface rheology instead modulates the style of material transfer: strong interfaces favor clustered, punctuated exhumation events, whereas weak interfaces promote more continuous exhumation (Figure 9). Stagnation, instead, is almost always intermittent (Figure 10), with the exception of the uniform serpentinite case, which facilitates continuous stagnation but triggers extreme crustal thickening. As with exhumation, stagnation within the subduction channel generally coincides with or follows dynamic slowdown, though it may initiate earlier depending on sediment supply, crustal thickening, and the presence of serpentinite.

To better understand the time evolution of exhumation in our models, we conduct a simplified analytical force balance calculation to evaluate the relative balance between the up-directed buoyancy stress of a package of basalt, σ_b, and the downwards-directed shear stress, τ, exerted on the base of the interface by the slab (cf. England & Smye, 2023). In our formulation, which is detailed in Text S1 in Supporting Information S1, σ_b is constant, while τ scales with convergence rate and hence evolves through time. Exhumation is deemed viable when the buoyancy stress σ_b exceeds the shear stress τ acting on a rock package. Although our system includes localized shear zones, different lithologies with complex flow laws, and hence an overall more complex force balance, this provides a useful first-order estimate of when exhumation should initiate. Applying this approach to basalt in our models (Text S1, Figure S18 in Supporting Information S1), we find that the $\sigma_b > \tau$ condition is only briefly met during initial subduction, and is then steadily maintained after slowdown, when τ decreases from >20 MPa to ∼8 MPa and becomes lower than σ_b (12 MPa). This simple estimate is consistent with the onset of stagnation and exhumation that we observe in our models. That is, basaltic crust can only exhume or stagnate when the downdragging shear stresses are sufficiently low during slow subduction, but does not require complete cessation of subduction. The negative buoyancy of eclogites, however, always promotes subduction, and the simple $\sigma_b > \tau$ criterion is therefore never satisfied. Instead, their stagnation in our models reflects the evolving mechanical coupling with the surrounding lithologies and the interface rheology, as detailed in Text S1 in Supporting Information S1. Hence, in our models, additional factors, such as interactions with surrounding lithologies, must operate to produce the observed eclogite stagnation.

A second, more extreme, velocity slowdown (i.e., kinematic slowdown) does not significantly alter the interface structure. The resulting reduction in basal traction, however, weakens corner flow at the base of the accretionary prism (Cloos, 1982; Platt, 1993), reducing exhumation volume as some previously exhumed particles are re-subducted following kinematic slowdown and the shut-down of corner flow. This effect is reduced in the 50% velocity model, where traction remains high enough to maintain some corner flow and continued exhumation of shallow, low-pressure material, as previously demonstrated in analytical and modeling studies (Allemand & Lardeaux, 1997; Cloos, 1982; Platt, 1993; Yamato et al., 2007). Despite reduced exhumation, stagnation increases across all depths under slower velocities (Figure 4c). In the prism, this reflects basal accretion (e.g., Ruh, 2020) and re-subduction and stagnation of particles that were partially exhumed during earlier times (Figure S10 in Supporting Information S1). Deeper in the interface, reduced shear stress increases coupling between slab and interface material (vs. decoupling at high strain rates; e.g., Duarte et al., 2015; Ruh et al., 2015; Yáñez & Cembrano, 2004). Under these conditions, the viscous traction exerted by the slab is insufficient to overcome the buoyancy of crustal lithologies (sediments and basalts), thereby favoring the stagnation of these units at depth. The resulting exhumation and stagnation patterns are then highly time-dependent, in broad agreement with inferences from the HP rock record in oceanic subduction settings (Agard et al., 2009, 2018).

Overall, our findings exhibit key differences relative to studies that either model exhumation under fixed convergence rates (e.g., Gerya et al., 2002; Ruh et al., 2015; Stöckhert & Gerya, 2005; Vaughan-Hammon et al., 2022; Wang et al., 2019) or incorporate only abrupt convergence rates changes (e.g., Vaughan-Hammon et al., 2022). These approaches typically generate exhumation during periods of constant convergence. In contrast, our models incorporate a time-dependent velocity evolution, which results in exhumation and stagnation of oceanic rocks that emerges during and after a phase of dynamic slowdown, without requiring complete cessation of subduction or an instantaneous, drastic reduction in convergence, as suggested in some previous studies (cf. England & Holland, 1979; England & Smye, 2023; Ernst, 1975; Platt, 1993). In particular, we find that

all exhumed particles detach from the slab within a narrow window around the dynamic slowdown event early in the subduction zone's lifetime. This indicates that exhumed rocks within our models capture a distinct, early-stage snapshot of the plate interface's evolution. Even during the near-constant velocity phase, exhumation and stagnation are controlled by shear zones developed during subduction infancy. Our models therefore indicate that the interface retains memory of its earlier deformation, and that both exhumation and stagnation are transient and rheology and history dependent processes.

4.3. Comparison With the Rock Record

Here we compare our model results with the properties of exhumation and underplating inferred from the rock record, focusing on the mechanisms of exhumation and underplating, as well as the timing of these processes within a subduction zone's lifetime. Two principal depth domains for material transfer and exhumation may be identified in oceanic subduction zones: (a) the accretionary prism, which comprises both shallow and intermediate levels of deformation, and (b) the deeper subduction channel.

Within the accretionary prisms (≤50 km depth), exhumation is commonly achieved through the offscraping, stacking, or basal accretion of metasedimentary nappes onto the overriding plate (e.g., Agard et al., 2009; Cloos & Shreve, 1988; Glodny et al., 2005; Tewksbury-Christle et al., 2021), as documented in the Chilean Coastal Cordillera (Glodny et al., 2005; Juez-Larré et al., 2010; Willner et al., 2004), the Western Alps (Agard et al., 2002, 2009; Federico et al., 2005), the Shimanto Belt (G. Kimura et al., 2012; Tagami et al., 1995; Wintsch et al., 1999), the Kamuikotan Belt (Takeshita et al., 2023), the Nankai Through (G. Kimura et al., 2018), Kodiak Island (Meneghini et al., 2009; Rajič et al., 2023; Sample & Moore, 1987), and the Olympic Mountains (Brandon et al., 1998). Within this domain, intermediate depths corresponding to epidote–blueschist facies conditions (0.8–1.3 GPa; ∼25–45 km), basal accretion represents a dynamic regime of both material transfer and exhumation within the subduction interface, where metasedimentary and basaltic units can be temporarily stored, reworked, and subsequently exhumed. The Western Alps provide a clear example of this intermediate-depth system, where units may experience prolonged residence within the channel before exhumation (e.g., Gyomlai et al., 2023).

Deeper in the subduction channel (≤150 km depth), slices of the slab top can detach and be underplated to the overriding plate through downstepping of the main shear zone (e.g., Bangs et al., 2020; Behr & Bürgmann, 2021; Kotowski et al., 2022; Poulaki et al., 2023; Ujiie et al., 2024). These underplated slices may later be re-exhumed during subsequent tectonic events such as slab breakoff, rollback, or continental collision (e.g., Agard et al., 2001). Such processes are widely recorded in high-pressure rocks within subduction complexes (Agard et al., 2018; Angiboust et al., 2014; Jolivet et al., 2005; Monie & Agard, 2009; Poulaki & Stockli, 2022). Examples include the Nevado-Filábride Complex (Poulaki et al., 2023), the Franciscan Complex (Wakabayashi, 2015), and the Cycladic Blueschist Unit (Kotowski et al., 2022).

While natural systems exhibit exhumation originating from both the accretionary prism and the subduction channel, exhumation in our models occurs within the accretionary prism, encompassing both shallow and intermediate levels (≤50 km; 0.8–1.3 GPa), while material entering the subduction channel is underplated rather than exhumed. Underplating occurs along much of the plate interface (≤140 km) and is sensitive to interface rheology and buoyancy, mirroring the spatially and temporally variable nature of underplating inferred from natural systems. Hence, while our models capture a two-level exhumation structure within the prism (shallow and intermediate) together with deep interface underplating inferred from the rock record, they do not reproduce deeper subduction-channel exhumation (e.g., eclogites),the implications of which are discussed in Section 4.4 in the context of the material properties of such dense lithologies.

Temporal constraints from the rock record provide further insight into exhumation and underplating. Exhumation of sedimentary material is typically prolonged, spanning periods of ∼25 Myr in the Alpine Schistes Lustrés (Guillot et al., 2009) to ∼100 Myr in Chile (Glodny et al., 2005). In contrast, exhumation of oceanic crustal rocks is generally punctuated and less than 20 Myr (Agard et al., 2009, 2018). It can occur early in the subduction history, as in the exhumation of metamorphic soles in Chile (Glodny et al., 2005); late, during the cessation of subduction, as in New Caledonia (Fitzherbert et al., 2005); or during ongoing subduction, as observed in Cuba (García-Casco et al., 2006), including within the Escambray dome, where multiple tectonic slices were emplaced during Late Cretaceous subduction (Despaigne Diaz et al., 2016; Schneider et al., 2004). Together, these observations highlight two end-member behaviors: longer, more continuous exhumation of sediments versus shorter, more episodic exhumation of oceanic crust. Our models also exhibit this contrast. Sediment exhumation

is more continuous and longer-lasting, whereas exhumation of oceanic crust is short-lived and punctuated, reflecting its stronger sensitivity to plate velocity–induced changes in slab–crust coupling (Figure 10). Despite this variability in timing, all exhumed rocks detach from the slab in a single, punctuated event, reflecting the transient character of plate interface deformation in the models. Consistent with rock record inferences, exhumed materials represent only a small fraction of the total volume of subducted crust (cf. ∼4% in our models and less than 5% in volume from Agard et al., 2009; Lallemand et al., 2024).

Underplating is inferred to typically last for tens of Myr. In the Franciscan Complex, for example, underplating is thought to last ∼10 Myr (Dumitru et al., 2010), 15 Myr in Zagros (Angiboust et al., 2016), and 60 Myr in the Nevado–Filábride Complex (Poulaki et al., 2023). In most cases, underplating is associated with rearrangements in regional tectonics (Agard et al., 2018; Ring & Layer, 2003; H. Kimura et al., 2010). Our models likewise produce underplating over multi-Myr intervals (∼15 Myr), but in a simplified context where the only driver of temporal variability is plate-velocity change. Thus, while the modeled durations of underplating fall within the natural range, the underlying drivers differ: in nature, additional factors such as tectonic reorganizations contribute to the timing, whereas in our models the temporal variability arises solely from plate velocity changes. Nevertheless, in both cases underplating is episodic and involves only a small fraction of the total subducted material, consistent with the punctuated, transient character of interface deformation highlighted by our modeling results.

4.4. Model Limitations and Future Outlook

While our models successfully reproduce the episodic nature of exhumation and underplating observed in the rock record, they exhibit limitations in capturing other key aspects.

Our reference model predicts peak *P–T* conditions of 1.2 GPa/200°C for exhumed particles and 2.5 GPa/450°C for stagnant ones (Figure 4), which are colder and lower pressure relative to average conditions reported from the rock record (e.g., Penniston-Dorland et al., 2015). Higher pressures (up to 3.5 GPa) can be achieved by introducing a weak serpentinite layer beneath the oceanic crust, but this leads to extreme crustal thickening of up to 50 km. Across all models, temperatures remain systematically colder than *P–T* estimates from rocks exhumed at oceanic subduction zones (Agard et al., 2018). Several mechanisms could contribute to this discrepancy, such as preferential exhumation during warmer stages of subduction (van Keken et al., 2018) and/or shear heating (England, 2018; Kohn et al., 2018), both of which are not considered in our idealized models. Another contributor is likely that our models assume an old, and therefore relatively cold, subducting plate (90 Myr). As a result, our results are most applicable to mature subduction systems, although a younger, warmer plate would likely shift *P–T* paths toward higher geothermal gradients and may impact exhumation and stagnation.

Moreover, our models only include the early stages of exhumation and stagnation, and fail to produce complete *P–T* loops (i.e., up to the surface). This is likely due to the absence of key shallow drivers of exhumation, such as erosion or extensional tectonics (e.g., Brun & Faccenna, 2008; Konstantinovskaia & Malavieille, 2005; Yamato et al., 2007), that would promote the transport these rocks to the surface. Without these processes, the overburden prevents rocks from reaching the surface. Furthermore, phase transitions in our work are simplified to only include eclogitization that occurs near-instantaneously in *P–T* space. Instead, oceanic crust undergoes a range of continuous and discontinuous reactions that alter the buoyancy and hydration state of the plate interface. Specifically, dehydration reactions release fluids that may alter the shear stress at the subduction interface and catalyze metamorphic reactions (Stöckhert, 2002). In natural systems, these fluids can also promote hydration and serpentinization of the mantle wedge, significantly weakening the interface and enhancing strain localization along the slab top (e.g., Guillot et al., 2009). Such hydration-driven weakening may further introduce feedbacks with subduction dynamics and convergence rates (Nakao et al., 2018; Stoner et al., 2025), processes that are not captured in our models. As a result, the overriding plate effectively behaves as a mechanically strong, non-hydrated boundary, and our results should be interpreted as a stiff-wedge end-member.

Notably, unlike the rock record, our models do not reproduce exhumation originating from deeper within the subduction channel, including eclogitic material, highlighting limitations of the current modeling approach. In natural systems, the exhumation of eclogites is facilitated by their mixing and emplacement into more buoyant phases, for example, through serpentinization following fluid release along the interface (e.g., Angiboust et al., 2012), or by the occurrence of anomalous events such as an entire rifted continental margin entering the subduction channel in the case of the Alps (Agard & Handy, 2021), none of which are adequately represented in

our setup. However, recent geological interpretations suggest that large coherent eclogite bodies (e.g., Zermatt–Saas) may represent an end-member condition rather than a typical feature of oceanic subduction, and may instead remain transiently stored and transported along a weak, hydrated plate interface until later tectonic reactivation enables final exhumation (Angiboust & Agard, 2010; Angiboust et al., 2009). In this view, the absence of early- or syn-subduction exhumation of such large bodies in our models is not unexpected. In addition, first-order limitations in surface exhumation can also be related to the timescales required for the development of large accretionary wedges capable of transporting material to the surface. As shown in previous work (Malavieille, 2010; Menant et al., 2020; Perrin et al., 2013), long-lived subduction permits the growth of large antiformal wedge stacks, where episodic basal accretion events ("basal kicks") drive incremental upward motion of accreted material across the forearc. Such processes, together with erosion and extensional deformation, are not included in our setup. Consequently, while the models capture the transient and localized nature of underplating and shallow exhumation, they do not reproduce deep eclogitic exhumation.

Our findings emphasize that a time-dependent plate velocity structure imparts an important control on the punctuated exhumation and underplating observed in the rock record. Future work on exhumation could be refined by integrating shear heating, tectonic processes such as extension, rollback, and fluid release along the subduction interface. As most of these processes are also time-dependent—for example, shear heating depends on evolving plate velocities—coupling them with our approach could provide further insights into the episodic nature of exhumation and underplating.

5. Conclusions

Overall, our modeling results demonstrate that time-dependent variations in plate velocity alone can generate punctuated exhumation and underplating throughout the lifetime of a subduction zone. To explore the impact of this, we examined the impact of such temporal variations on exhumation and underplating within kinematically driven numerical subduction models. To account for the mechanical variability of plate interfaces worldwide, we also conducted rheological and compositional tests to assess their influence on exhumation.

In our models, exhumation and underplating are episodic and tightly coupled to convergence rate changes. Exhumation initiates when convergence decreases below 5 cm/yr and is consistently triggered by the initial plate slowdown event associated with slab interaction with the lower mantle; all exhumed particles detaching from the slab at this stage. Exhumation is confined to the relatively shallow interface ($\leq$50 km depth), within the accretionary prism, and involves the decoupling of oceanic crust and sediments. Eclogites do not exhume, consistent with the need for additional processes—buoyant mixing, fluid weakening, or self-consistent serpentinization—not included in our baseline models. Stagnation also occurs as discontinuous pulses but, unlike exhumation, throughout the entire post-slowdown, evolution of the subduction zone. In addition to plate velocity evolution, our additional tests demonstrate how exhumation and stagnation volumes, styles, and timings also depend strongly on interface rheology and compositions.

Our models exhibit much of the punctuated interface deformation (exhumation and underplating) inferred from the geologic record, thereby demonstrating the impact of changes in plate velocity on these processes. This shows that even moderate, geologically reasonable changes in plate velocity are sufficient to drive the initial phases of exhumation and underplating, without the need to invoke more dramatic events such as slab break-off or subduction termination. Incorporating time-dependent velocity variations is therefore important for accurately capturing deformation and material recovery processes at subduction interfaces.

Conflict of Interest

The authors declare no conflicts of interest relevant to this study.

Availability Statement

The modified ASPECT version, mesh refinement plugin, input geometries and parameter files necessary to run the models can be found in the following Zenodo repository (Turino et al., 2026): https://doi.org/10.5281/zenodo.18249159.

Acknowledgments
We are grateful to the two anonymous reviewers for their helpful comments which improved the manuscript. We thank the Computational Infrastructure for Geodynamics (geodynamics.org) which is funded by the National Science Foundation under award EAR-0949446 and EAR-1550901 for supporting the development of ASPECT. AFH was partially supported by NSF EAR-2119842 and computational resources were provided through NSF ACCESS allocation EES-220058.

References

Abila, A. L., Behr, W. M., & Ruh, J. (2025). Strength of viscous subduction interfaces: A global compilation. *Geology*, *53*(2), 105–108. https://doi.org/10.1130/g52518.1

Agard, P., & Handy, M. R. (2021). Ocean subduction dynamics in the alps. Elements: An international magazine of mineralogy. *Geochemistry, and Petrology*, *17*(1), 9–16.

Agard, P., Jolivet, L., & Goffe, B. (2001). Tectonometamorphic evolution of the Schistes Lustres Complex; implications for the exhumation of HP and UHP rocks in the western alps. *Bulletin de la Societe Geologique de France*, *172*(5), 617–636. https://doi.org/10.2113/172.5.617

Agard, P., Monié, P., Jolivet, L., & Goffé, B. (2002). Exhumation of the Schistes Lustrés Complex: In situ laser probe $^{40}Ar/^{39}Ar$ constraints and implications for the western alps. *Journal of Metamorphic Geology*, *20*(6), 599–618. https://doi.org/10.1046/j.1525-1314.2002.00391.x

Agard, P., Plunder, A., Angiboust, S., Bonnet, G., & Ruh, J. (2018). The subduction plate interface: Rock record and mechanical coupling (from long to short timescales). *Lithos*, *320*, 537–566. https://doi.org/10.1016/j.lithos.2018.09.029

Agard, P., Yamato, P., Jolivet, L., & Burov, E. (2009). Exhumation of oceanic blueschists and eclogites in subduction zones: Timing and mechanisms. *Earth-Science Reviews*, *92*(1–2), 53–79. https://doi.org/10.1016/j.earscirev.2008.11.002

Allemand, P., & Lardeaux, J.-M. (1997). Strain partitioning and metamorphism in a deformable orogenic wedge: Application to the alpine belt. *Tectonophysics*, *280*(1–2), 157–169. https://doi.org/10.1016/s0040-1951(97)00136-4

Angiboust, S., & Agard, P. (2010). Initial water budget: The key to detaching large volumes of eclogitized oceanic crust along the subduction channel? *Lithos*, *120*(3–4), 453–474. https://doi.org/10.1016/j.lithos.2010.09.007

Angiboust, S., Agard, P., Glodny, J., Omrani, J., & Oncken, O. (2016). Zagros blueschists: Episodic underplating and long-lived cooling of a subduction zone. *Earth and Planetary Science Letters*, *443*, 48–58. https://doi.org/10.1016/j.epsl.2016.03.017

Angiboust, S., Agard, P., Jolivet, L., & Beyssac, O. (2009). The Zermatt-Saas Ophiolite: The largest (60-km wide) and deepest (c. 70–80 km) continuous slice of oceanic lithosphere detached from a subduction zone? *Terra Nova*, *21*(3), 171–180. https://doi.org/10.1111/j.1365-3121.2009.00870.x

Angiboust, S., Agard, P., Raimbourg, H., Yamato, P., & Huet, B. (2011). Subduction interface processes recorded by eclogite-facies shear zones (Monviso, W. Alps). *Lithos*, *127*(1–2), 222–238. https://doi.org/10.1016/j.lithos.2011.09.004

Angiboust, S., & Glodny, J. (2020). Exhumation of eclogitic ophiolitic nappes in the W. Alps: New age data and implications for crustal wedge dynamics. *Lithos*, *356*, 105374. https://doi.org/10.1016/j.lithos.2020.105374

Angiboust, S., Glodny, J., Oncken, O., & Chopin, C. (2014). In search of transient subduction interfaces in the Dent Blanche–Sesia Tectonic System (W. Alps). *Lithos*, *205*, 298–321. https://doi.org/10.1016/j.lithos.2014.07.001

Angiboust, S., Menant, A., Gerya, T., & Oncken, O. (2022). The rise and demise of deep accretionary wedges: A long-term field and numerical modeling perspective. *Geosphere*, *18*(1), 69–103. https://doi.org/10.1130/ges02392.1

Angiboust, S., Wolf, S., Burov, E., Agard, P., & Yamato, P. (2012). Effect of fluid circulation on subduction interface tectonic processes: Insights from thermo-mechanical numerical modelling. *Earth and Planetary Science Letters*, *357*, 238–248. https://doi.org/10.1016/j.epsl.2012.09.012

Bangerth, W., Dannberg, J., Fraters, M., Gassmoeller, R., Glerum, A., Heister, T., et al. (2023). Geodynamics/aspect: Aspect 2.5.0.

Bangs, N. L., Morgan, J., Tréhu, A., Contreras-Reyes, E., Arnulf, A., Han, S., et al. (2020). Basal accretion along the south central Chilean margin and its relationship to great earthquakes. *Journal of Geophysical Research: Solid Earth*, *125*(11), e2020JB019861. https://doi.org/10.1029/2020jb019861

Beaumont, C., Ellis, S., & Pfiffner, A. (1999). Dynamics of sediment subduction-accretion at convergent margins: Short-term modes, long-term deformation, and tectonic implications. *Journal of Geophysical Research*, *104*(B8), 17573–17601. https://doi.org/10.1029/1999jb900136

Bebout, G. E., & Penniston-Dorland, S. C. (2016). Fluid and mass transfer at subduction interfaces—The field metamorphic record. *Lithos*, *240*, 228–258. https://doi.org/10.1016/j.lithos.2015.10.007

Behr, W. M., & Becker, T. W. (2018). Sediment control on subduction plate speeds. *Earth and Planetary Science Letters*, *502*, 166–173. https://doi.org/10.1016/j.epsl.2018.08.057

Behr, W. M., & Bürgmann, R. (2021). What's down there? The structures, materials and environment of deep-seated slow slip and tremor. *Philosophical Transactions of the Royal Society A*, *379*(2193), 20200218. https://doi.org/10.1098/rsta.2020.0218

Behr, W. M., & Platt, J. P. (2013). Rheological evolution of a mediterranean subduction complex. *Journal of Structural Geology*, *54*, 136–155. https://doi.org/10.1016/j.jsg.2013.07.012

Bellot, J.-P., & Roig, J.-Y. (2007). Episodic exhumation of HP rocks inferred from structural data and PT paths from the southwestern Massif Central (Variscan Belt, France). *Journal of Structural Geology*, *29*(9), 1538–1557. https://doi.org/10.1016/j.jsg.2007.04.001

Bermúdez, M., Hoorn, C., Bernet, M., Carrillo, E., Van Der Beek, P., Garver, J., et al. (2017). The detrital record of late-miocene to pliocene surface uplift and exhumation of the Venezuelan Andes in the Maracaibo and Barinas foreland basins. *Basin Research*, *29*(S1), 370–395. https://doi.org/10.1111/bre.12154

Brandon, M. T., Roden-Tice, M. K., & Garver, J. I. (1998). Late Cenozoic exhumation of the Cascadia accretionary wedge in the Olympic Mountains, Northwest Washington State. *Geological Society of America Bulletin*, *110*(8), 985–1009. https://doi.org/10.1130/0016-7606(1998)110<0985:lceotc>2.3.co;2

Brizzi, S., Becker, T. W., Faccenna, C., Behr, W., van Zelst, I., Dal Zilio, L., & van Dinther, Y. (2021). The role of sediment accretion and buoyancy on subduction dynamics and geometry. *Geophysical Research Letters*, *48*(20), e2021GL096266. https://doi.org/10.1029/2021gl096266

Brun, J.-P., & Faccenna, C. (2008). Exhumation of high-pressure rocks driven by slab rollback. *Earth and Planetary Science Letters*, *272*(1–2), 1–7. https://doi.org/10.1016/j.epsl.2008.02.038

Burov, E., Jolivet, L., Le Pourhiet, L., & Poliakov, A. (2001). A thermomechanical model of exhumation of high pressure (Hp) and ultra-high pressure (UHP) metamorphic rocks in alpine-type collision belts. *Tectonophysics*, *342*(1–2), 113–136. https://doi.org/10.1016/s0040-1951(01)00158-5

Cannat, M., Mevel, C., Maia, M., Deplus, C., Durand, C., Gente, P., et al. (1995). Thin crust, ultramafic exposures, and rugged faulting patterns at the mid-Atlantic ridge (22–24 N). *Geology*, *23*(1), 49–52. https://doi.org/10.1130/0091-7613(1995)023<0049:tcuear>2.3.co;2

Cerpa, N. G., Hassani, R., Gerbault, M., & Prévost, J.-H. (2014). A fictitious domain method for lithosphere-asthenosphere interaction: Application to periodic slab folding in the upper mantle. *Geochemistry, Geophysics, Geosystems*, *15*(5), 1852–1877. https://doi.org/10.1002/2014gc005241

Chemenda, A. I., Mattauer, M., Malavieille, J., & Bokun, A. N. (1995). A mechanism for syn-collisional rock exhumation and associated normal faulting: Results from physical modelling. *Earth and Planetary Science Letters*, *132*(1–4), 225–232. https://doi.org/10.1016/0012-821x(95)00042-b

Cloos, M. (1982). Flow melanges: Numerical modeling and geologic constraints on their origin in the Franciscan Subduction Complex, California. *Geological Society of America Bulletin*, *93*(4), 330–345. https://doi.org/10.1130/0016-7606(1982)93<330:fmnmag>2.0.co;2

Cloos, M., & Shreve, R. L. (1988). Subduction-channel model of prism accretion, melange formation, sediment subduction, and subduction erosion at convergent plate margins: 1. Background and description. *Pure and Applied Geophysics*, *128*(3–4), 455–500. https://doi.org/10.1007/bf00874548

Coleman, R., & Lanphere, M. A. (1971). Distribution and age of high-grade blueschists, associated eclogites, and amphibolites from Oregon and California. *Geological Society of America Bulletin*, *82*(9), 2397–2412. https://doi.org/10.1130/0016-7606(1971)82[2397:daaohb]2.0.co;2

Cowan, D. S., & Silling, R. M. (1978). A dynamic, scaled model of accretion at trenches and its implications for the tectonic evolution of subduction complexes. *Journal of Geophysical Research*, *83*(B11), 5389–5396. https://doi.org/10.1029/jb083ib11p05389

Croon, M. B., Cande, S. C., & Stock, J. M. (2008). Revised Pacific-Antarctic Plate motions and geophysics of the Menard Fracture Zone. *Geochemistry, Geophysics, Geosystems*, *9*(7). https://doi.org/10.1029/2008gc002019

den Hartog, S. A., & Spiers, C. J. (2013). Influence of subduction zone conditions and gouge composition on frictional slip stability of megathrust faults. *Tectonophysics*, *600*, 75–90. https://doi.org/10.1016/j.tecto.2012.11.006

Despaigne Diaz, A. I., Garcia Casco, A., & Caceres Govea, D. (2016). Accretionary complexes of Cuba, with emphasis on the escambray complex (central Cuba). In *Geological society of America abstracts* (Vol. 48, p. 282164).

Dragovic, B., Angiboust, S., & Tappa, M. J. (2020). Petrochronological close-up on the thermal structure of a paleo-subduction zone (W. Alps). *Earth and Planetary Science Letters*, *547*, 116446. https://doi.org/10.1016/j.epsl.2020.116446

Drucker, D. C., & Prager, W. (1952). Soil mechanics and plastic analysis or limit design. *Quarterly of Applied Mathematics*, *10*(2), 157–165. https://doi.org/10.1090/qam/48291

Duarte, J. C., Schellart, W. P., & Cruden, A. R. (2015). How weak is the subduction zone interface? *Geophysical Research Letters*, *42*(8), 2664–2673. https://doi.org/10.1002/2014gl062876

Dumitru, T. A., Wakabayashi, J., Wright, J. E., & Wooden, J. L. (2010). Early cretaceous transition from nonaccretionary behavior to strongly accretionary behavior within the Franciscan Subduction Complex. *Tectonics*, *29*(5). https://doi.org/10.1029/2009tc002542

Duretz, T., Gerya, T. V., & May, D. A. (2011). Numerical modelling of spontaneous slab breakoff and subsequent topographic response. *Tectonophysics*, *502*(1–2), 244–256. https://doi.org/10.1016/j.tecto.2010.05.024

Duretz, T., Schmalholz, S., & Gerya, T. (2012). Dynamics of slab detachment. *Geochemistry, Geophysics, Geosystems*, *13*(3). https://doi.org/10.1029/2011gc004024

Ellis, S., Beaumont, C., & Pfiffner, O. A. (1999). Geodynamic models of crustal-scale episodic tectonic accretion and underplating in subduction zones. *Journal of Geophysical Research*, *104*(B7), 15169–15190. https://doi.org/10.1029/1999jb900071

England, P. C. (2018). On shear stresses, temperatures, and the maximum magnitudes of earthquakes at convergent plate boundaries. *Journal of Geophysical Research: Solid Earth*, *123*(8), 7165–7202. https://doi.org/10.1029/2018jb015907

England, P. C., & Holland, T. J. (1979). Archimedes and the Tauern Eclogites: The role of buoyancy in the preservation of exotic eclogite blocks. *Earth and Planetary Science Letters*, *44*(2), 287–294. https://doi.org/10.1016/0012-821x(79)90177-8

England, P. C., & Smye, A. J. (2023). Metamorphism and deformation on subduction interfaces: 1. Physical framework. *Geochemistry, Geophysics, Geosystems*, *24*(1), e2022GC010644. https://doi.org/10.1029/2022gc010644

Enns, A., Becker, T. W., & Schmeling, H. (2005). The dynamics of subduction and trench migration for viscosity stratification. *Geophysical Journal International*, *160*(2), 761–775. https://doi.org/10.1111/j.1365-246x.2005.02519.x

Ernst, W. (1970). Tectonic contact between the Franciscan mélange and the Great Valley sequence—Crustal expression of a late Mesozoic Benioff zone. *Journal of Geophysical Research*, *75*(5), 886–901. https://doi.org/10.1029/jb075i005p00886

Ernst, W. (1975). Systematics of large-scale tectonics and age progressions in Alpine and Circum-Pacific blueschist belts. *Tectonophysics*, *26*(3–4), 229–246. https://doi.org/10.1016/0040-1951(75)90092-x

Ernst, W. (1988). Tectonic history of subduction zones inferred from retrograde blueschist PT paths. *Geology*, *16*(12), 1081–1084. https://doi.org/10.1130/0091-7613(1988)016<1081:thoszi>2.3.co;2

Ernst, W., Maruyama, S., & Wallis, S. (1997). Buoyancy-driven, rapid exhumation of ultrahigh-pressure metamorphosed continental crust. *Proceedings of the National Academy of Sciences*, *94*(18), 9532–9537. https://doi.org/10.1073/pnas.94.18.9532

Faccenda, M., Gerya, T. V., & Chakraborty, S. (2008). Styles of post-subduction collisional orogeny: Influence of convergence velocity, crustal rheology and radiogenic heat production. *Lithos*, *103*(1–2), 257–287. https://doi.org/10.1016/j.lithos.2007.09.009

Faccenna, C., Heuret, A., Funiciello, F., Lallemand, S., & Becker, T. W. (2007). Predicting trench and plate motion from the dynamics of a strong slab. *Earth and Planetary Science Letters*, *257*(1–2), 29–36. https://doi.org/10.1016/j.epsl.2007.02.016

Fassoulas, C., Kilias, A., & Mountrakis, D. (1994). Postnappe stacking extension and exhumation of high-pressure/low-temperature rocks in the Island of Crete, Greece. *Tectonics*, *13*(1), 127–138. https://doi.org/10.1029/93tc01955

Federico, L., Capponi, G., Crispini, L., Scambelluri, M., & Villa, I. M. (2005). $^{39}Ar/^{40}Ar$ dating of high-pressure rocks from the Ligurian alps: Evidence for a continuous subduction–exhumation cycle. *Earth and Planetary Science Letters*, *240*(3–4), 668–680. https://doi.org/10.1016/j.epsl.2005.09.062

Federico, L., Crispini, L., Scambelluri, M., & Capponi, G. (2007). Ophiolite mélange zone records exhumation in a fossil subduction channel. *Geology*, *35*(6), 499–502. https://doi.org/10.1130/g23190a.1

Fitzherbert, J., Clarke, G., & Powell, R. (2005). Preferential retrogression of high-p metasediments and the preservation of blueschist to eclogite facies metabasite during exhumation, diahot terrane, NE New Caledonia. *Lithos*, *83*(1–2), 67–96. https://doi.org/10.1016/j.lithos.2005.01.005

Gao, X., & Wang, K. (2014). Strength of stick-slip and creeping subduction megathrusts from heat flow observations. *Science*, *345*(6200), 1038–1041. https://doi.org/10.1126/science.1255487

García-Casco, A., Torres-Roldán, R., Vinent, M. A. I., Millán, G., Cambra, K. N., Lázaro, C., & Vega, A. R. (2006). High pressure metamorphism of ophiolites in Cuba. *Geológica Acta: An International Earth Science Journal*, *4*(1), 63–88.

Garrido, C. J., Gueydan, F., Booth-Rea, G., Precigout, J., Hidas, K., Padrón-Navarta, J. A., & Marchesi, C. (2011). Garnet lherzolite and garnet-spinel mylonite in the Ronda peridotite: Vestiges of Oligocene backarc mantle lithospheric extension in the western Mediterranean. *Geology*, *39*(10), 927–930. https://doi.org/10.1130/g31760.1

Gassmöller, R., Lokavarapu, H., Heien, E., Puckett, E. G., & Bangerth, W. (2018). Flexible and scalable particle-in-cell methods with adaptive mesh refinement for geodynamic computations. *Geochemistry, Geophysics, Geosystems*, *19*(9), 3596–3604. https://doi.org/10.1029/2018gc007508

Gerya, T. V., Stöckhert, B., & Perchuk, A. L. (2002). Exhumation of high-pressure metamorphic rocks in a subduction channel: A numerical simulation. *Tectonics*, *21*(6), 6-1–6-19. https://doi.org/10.1029/2002tc001406

Giunchi, C., & Ricard, Y. (1999). High-pressure/low-temperature metamorphism and the dynamics of an accretionary wedge. *Geophysical Journal International*, *136*(3), 620–628. https://doi.org/10.1046/j.1365-246x.1999.00759.x

Glerum, A., Thieulot, C., Fraters, M., Blom, C., & Spakman, W. (2018). Nonlinear viscoplasticity in aspect: Benchmarking and applications to subduction. *Solid Earth*, *9*(2), 267–294. https://doi.org/10.5194/se-9-267-2018

Glodny, J., Lohrmann, J., Echtler, H., Gräfe, K., Seifert, W., Collao, S., & Figueroa, O. (2005). Internal dynamics of a paleoaccretionary wedge: Insights from combined isotope tectonochronology and sandbox modelling of the south-central Chilean forearc. *Earth and Planetary Science Letters*, *231*(1–2), 23–39. https://doi.org/10.1016/j.epsl.2004.12.014

Gorczyk, W., Guillot, S., Gerya, T. V., & Hattori, K. (2007). Asthenospheric upwelling, oceanic slab retreat, and exhumation of UHP mantle rocks: Insights from Greater Antilles. *Geophysical Research Letters*, *34*(21). https://doi.org/10.1029/2007gl031059

Grima, A. G., & Becker, T. W. (2024). The role of continental heterogeneity on the evolution of continental plate margin topography at subduction zones. *Earth and Planetary Science Letters*, *642*, 118856. https://doi.org/10.1016/j.epsl.2024.118856

Guillot, S., Hattori, K., Agard, P., Schwartz, S., & Vidal, O. (2009). Exhumation processes in oceanic and continental subduction contexts: A review. In *Subduction zone geodynamics* (pp. 175–205).

Gyomlai, T., Agard, P., Herviou, C., Jolivet, L., Monié, P., Mendes, K., & Iemmolo, A. (2023). In situ Rb–Sr and ^{40}Ar–^{39}Ar dating of distinct mica generations in the exhumed subduction complex of the western alps. *Contributions to Mineralogy and Petrology*, *178*(9), 58. https://doi.org/10.1007/s00410-023-02042-8

Hacker, B. R., Abers, G. A., & Peacock, S. M. (2003). Subduction factory 1. Theoretical mineralogy, densities, seismic wave speeds, and H_2O contents. *Journal of Geophysical Research*, *108*(B1). https://doi.org/10.1029/2001jb001127

Hacker, B. R., & Gerya, T. V. (2013). Paradigms, new and old, for ultrahigh-pressure tectonism. *Tectonophysics*, *603*, 79–88. https://doi.org/10.1016/j.tecto.2013.05.026

Heister, T., Dannberg, J., Gassmöller, R., & Bangerth, W. (2017). High accuracy mantle convection simulation through modern numerical methods–II: Realistic models and problems. *Geophysical Journal International*, *210*(2), 833–851. https://doi.org/10.1093/gji/ggx195

Hermann, J., Müntener, O., & Scambelluri, M. (2000). The importance of serpentinite mylonites for subduction and exhumation of oceanic crust. *Tectonophysics*, *327*(3–4), 225–238. https://doi.org/10.1016/s0040-1951(00)00171-2

Hilairet, N., Reynard, B., Wang, Y., Daniel, I., Merkel, S., Nishiyama, N., & Petitgirard, S. (2007). High-pressure creep of serpentine, interseismic deformation, and initiation of subduction. *Science*, *318*(5858), 1910–1913. https://doi.org/10.1126/science.1148494

Hirth, G., & Kohlstedt, D. (2003). Rheology of the upper mantle and the mantle wedge: A view from the experimentalists. In *Geophysical monograph-American geophysical union* (Vol. 138, pp. 83–106).

Holt, A. F., Becker, T., & Buffett, B. (2015). Trench migration and overriding plate stress in dynamic subduction models. *Geophysical Journal International*, *201*(1), 172–192. https://doi.org/10.1093/gji/ggv011

Holt, A. F., & Condit, C. B. (2021). Slab temperature evolution over the lifetime of a subduction zone. *Geochemistry, Geophysics, Geosystems*, *22*(6), e2020GC009476. https://doi.org/10.1029/2020gc009476

Jin, Z.-M., Zhang, J., Green, H., & Jin, S. (2001). Eclogite rheology: Implications for subducted lithosphere. *Geology*, *29*(8), 667–670. https://doi.org/10.1130/0091-7613(2001)029<0667:erifsl>2.0.co;2

Jolivet, L., Faccenna, C., Goffé, B., Burov, E., & Agard, P. (2003). Subduction tectonics and exhumation of high-pressure metamorphic rocks in the Mediterranean Orogens. *American Journal of Science*, *303*(5), 353–409.

Jolivet, L., Raimbourg, H., Labrousse, L., Avigad, D., Leroy, Y., Austrheim, H., & Andersen, T. B. (2005). Softening trigerred by eclogitization, the first step toward exhumation during continental subduction. *Earth and Planetary Science Letters*, *237*(3–4), 532–547. https://doi.org/10.1016/j.epsl.2005.06.047

Juez-Larré, J., Kukowski, N., Dunai, T. J., Hartley, A. J., & Andriessen, P. A. (2010). Thermal and exhumation history of the coastal cordillera arc of northern Chile revealed by thermochronological dating. *Tectonophysics*, *495*(1–2), 48–66. https://doi.org/10.1016/j.tecto.2010.06.018

Kerswell, B. C., Kohn, M. J., & Gerya, T. V. (2023). Computing rates and distributions of rock recovery in subduction zones. *Geochemistry, Geophysics, Geosystems*, *24*(5), e2022GC010834. https://doi.org/10.1029/2022gc010834

Kimura, G., Koge, H., & Tsuji, T. (2018). Punctuated growth of an accretionary prism and the onset of a seismogenic megathrust in the Nankai Trough. *Progress in Earth and Planetary Science*, *5*(1), 1–12. https://doi.org/10.1186/s40645-018-0234-1

Kimura, G., Yamaguchi, A., Hojo, M., Kitamura, Y., Kameda, J., Ujiie, K., et al. (2012). Tectonic mélange as fault rock of subduction plate boundary. *Tectonophysics*, *568*, 25–38. https://doi.org/10.1016/j.tecto.2011.08.025

Kimura, H., Takeda, T., Obara, K., & Kasahara, K. (2010). Seismic evidence for active underplating below the megathrust earthquake zone in Japan. *Science*, *329*(5988), 210–212. https://doi.org/10.1126/science.1187115

Kohn, M. J., Castro, A. E., Kerswell, B. C., Ranero, C. R., & Spear, F. S. (2018). Shear heating reconciles thermal models with the metamorphic rock record of subduction. *Proceedings of the National Academy of Sciences*, *115*(46), 11706–11711. https://doi.org/10.1073/pnas.1809962115

Konstantinovskaia, E., & Malavieille, J. (2005). Erosion and exhumation in accretionary orogens: Experimental and geological approaches. *Geochemistry, Geophysics, Geosystems*, *6*(2). https://doi.org/10.1029/2004gc000794

Kotowski, A. J., Cisneros, M., Behr, W. M., Stockli, D. F., Soukis, K., Barnes, J. D., & Ortega-Arroyo, D. (2022). Subduction, underplating, and return flow recorded in the cycladic blueschist unit exposed on Syros, Greece. *Tectonics*, *41*(6), e2020TC006528. https://doi.org/10.1029/2020tc006528

Koyama, Y., Wallis, S. R., & Nagaya, T. (2024). Subduction plate interface shear stress associated with rapid subduction at deep slow earthquake depths: Example from the Sanbagawa Belt, southwestern Japan. *Solid Earth*, *15*(2), 143–166. https://doi.org/10.5194/se-15-143-2024

Krebs, M., Schertl, H.-P., Maresch, W., & Draper, G. (2011). Mass flow in serpentinite-hosted subduction channels: P–T–t path patterns of metamorphic blocks in the Rio San Juan mélange (Dominican Republic). *Journal of Asian Earth Sciences*, *42*(4), 569–595. https://doi.org/10.1016/j.jseaes.2011.01.011

Krohe, A., & Mposkos, E. (2002). Multiple generations of extensional detachments in the Rhodope Mountains (northern Greece): Evidence of episodic exhumation of high-pressure rocks. In *The timing and location of major ore deposits in an evolving orogen*. Geological Society of London.

Kronbichler, M., Heister, T., & Bangerth, W. (2012). High accuracy mantle convection simulation through modern numerical methods. *Geophysical Journal International*, *191*(1), 12–29. https://doi.org/10.1111/j.1365-246x.2012.05609.x

Kukowski, N., Lallemand, S. E., Malavieille, J., Gutscher, M.-A., & Reston, T. J. (2002). Mechanical decoupling and basal duplex formation observed in sandbox experiments with application to the western Mediterranean ridge accretionary complex. *Marine Geology*, *186*(1–2), 29–42. https://doi.org/10.1016/s0025-3227(02)00171-8

Lallemand, S., Heuret, A., & Boutelier, D. (2005). On the relationships between slab dip, back-arc stress, upper plate absolute motion, and crustal nature in subduction zones. *Geochemistry, Geophysics, Geosystems*, *6*(9). https://doi.org/10.1029/2005gc000917

Lallemand, S., Peyret, M., Arcay, D., & Heuret, A. (2024). Accretion versus erosion and sediment transfer balance near the subduction interface. *Comptes Rendus Geoscience*, *356*(S2), 27–51. https://doi.org/10.5802/crgeos.252

Lamb, S. (2006). Shear stresses on megathrusts: Implications for mountain building behind subduction zones. *Journal of Geophysical Research*, *111*(B7). https://doi.org/10.1029/2005jb003916

Laurent, V., Jolivet, L., Roche, V., Augier, R., Scaillet, S., & Cardello, G. L. (2016). Strain localization in a fossilized subduction channel: Insights from the Cycladic Blueschist unit (Syros, Greece). *Tectonophysics*, *672*, 150–169. https://doi.org/10.1016/j.tecto.2016.01.036

Mackwell, S., Zimmerman, M., & Kohlstedt, D. (1998). High-temperature deformation of dry diabase with application to tectonics on Venus. *Journal of Geophysical Research*, *103*(B1), 975–984. https://doi.org/10.1029/97jb02671

Malatesta, C., Gerya, T., Scambelluri, M., Federico, L., Crispini, L., & Capponi, G. (2012). Intraoceanic subduction of "heterogeneous" oceanic lithosphere in narrow basins: 2d numerical modeling. *Lithos*, *140*, 234–251. https://doi.org/10.1016/j.lithos.2012.01.003

Malavieille, J. (2010). Impact of erosion, sedimentation, and structural heritage on the structure and kinematics of orogenic wedges: Analog models and case studies. *GSA Today*, *20*(1), 4–10. https://doi.org/10.1130/gsatg48a.1

Martinod, J., Funiciello, F., Faccenna, C., Labanieh, S., & Regard, V. (2005). Dynamical effects of subducting ridges: Insights from 3-d laboratory models. *Geophysical Journal International*, *163*(3), 1137–1150. https://doi.org/10.1111/j.1365-246x.2005.02797.x

Maruyama, S., & Parkinson, C. (2000). Overview of the geology, petrology and tectonic framework of the high-pressure–ultrahigh-pressure metamorphic belt of the Kokchetav Massif, Kazakhstan. *Island Arc*, *9*(3), 439–455. https://doi.org/10.1046/j.1440-1738.2000.00288.x

Menant, A., Angiboust, S., & Gerya, T. (2019). Stress-driven fluid flow controls long-term megathrust strength and deep accretionary dynamics. *Scientific Reports*, *9*(1), 9714. https://doi.org/10.1038/s41598-019-46191-y

Menant, A., Angiboust, S., Gerya, T., Lacassin, R., Simoes, M., & Grandin, R. (2020). Transient stripping of subducting slabs controls periodic forearc uplift. *Nature Communications*, *11*(1), 1823. https://doi.org/10.1038/s41467-020-15580-7

Meneghini, F., Marroni, M., Moore, J., Pandolfi, L., & Rowe, C. (2009). The processes of underthrusting and underplating in the geologic record: Structural diversity between the Franciscan Complex (California), The Kodiak Complex (Alaska) and The Internal Ligurian Units (Italy). *Geological Journal*, *44*(2), 126–152. https://doi.org/10.1002/gj.1144

Minnaert, C., Angiboust, S., Cambeses, A., Glodny, J., Muñoz-Montecinos, J., & Garcia-Casco, A. (2024). Omphacitite formation and fluid-rock interaction processes in an intra-slab eclogite-facies shear zone. *Lithos*, *484*, 107738. https://doi.org/10.1016/j.lithos.2024.107738

Monie, P., & Agard, P. (2009). Coeval blueschist exhumation along thousands of kilometers: Implications for subduction channel processes. *Geochemistry, Geophysics, Geosystems*, *10*(7). https://doi.org/10.1029/2009gc002428

Moore, J. C. (1989). Tectonics and hydrogeology of accretionary prisms: Role of the décollement zone. *Journal of Structural Geology*, *11*(1–2), 95–106. https://doi.org/10.1016/0191-8141(89)90037-0

Muller, M., Robinson, C., Minshull, T., White, R., & Bickle, M. (1997). Thin crust beneath ocean drilling program borehole 735b at the southwest Indian Ridge? *Earth and Planetary Science Letters*, *148*(1–2), 93–107. https://doi.org/10.1016/s0012-821x(97)00030-7

Muñoz-Montecinos, J., Angiboust, S., Garcia-Casco, A., Glodny, J., & Bebout, G. (2021). Episodic hydrofracturing and large-scale flushing along deep subduction interfaces: Implications for fluid transfer and carbon recycling (Zagros Orogen, southeastern Iran). *Chemical Geology*, *571*, 120173. https://doi.org/10.1016/j.chemgeo.2021.120173

Nakao, A., Iwamori, H., Nakakuki, T., Suzuki, Y. J., & Nakamura, H. (2018). Roles of hydrous lithospheric mantle in deep water transportation and subduction dynamics. *Geophysical Research Letters*, *45*(11), 5336–5343. https://doi.org/10.1029/2017gl076953

Neuharth, D., Behr, W. M., & Holt, A. F. (2026). The role of along-strike variations in interface rheology on subduction dynamics: Constraints from three-dimensional numerical models. *Geophysical Journal International*, *244*(3), ggaf515. https://doi.org/10.1093/gji/ggaf515

Pagé, L., & Hattori, K. (2019). Abyssal serpentinites: Transporting halogens from Earth's surface to the deep mantle. *Minerals*, *9*(1), 61. https://doi.org/10.3390/min9010061

Peacock, S. M. (1992). Blueschist-facies metamorphism, shear heating, and P-T-t paths in subduction shear zones. *Journal of Geophysical Research*, *97*(B12), 17693–17707. https://doi.org/10.1029/92jb01768

Penniston-Dorland, S. C., Kohn, M. J., & Manning, C. E. (2015). The global range of subduction zone thermal structures from exhumed blueschists and eclogites: Rocks are hotter than models. *Earth and Planetary Science Letters*, *428*, 243–254. https://doi.org/10.1016/j.epsl.2015.07.031

Perrin, C., Clemenzi, L., Malavieille, J., Molli, G., Taboada, A., & Dominguez, S. (2013). Impact of erosion and décollements on large-scale faulting and folding in orogenic wedges: Analogue models and case studies. *Journal of the Geological Society*, *170*(6), 893–904. https://doi.org/10.1144/jgs2013-012

Philippot, P., & van Roermund, H. L. (1992). Deformation processes in eclogitic rocks: Evidence for the rheological delamination of the oceanic crust in deeper levels of subduction zones. *Journal of Structural Geology*, *14*(8–9), 1059–1077. https://doi.org/10.1016/0191-8141(92)90036-v

Platt, J. (1975). Metamorphic and deformational processes in the Franciscan Complex, California: Some insights from the Catalina Schist Terrane. *Geological Society of America Bulletin*, *86*(10), 1337–1347. https://doi.org/10.1130/0016-7606(1975)86<1337:madpit>2.0.co;2

Platt, J. (1993). Mechanics of oblique convergence. *Journal of Geophysical Research*, *98*(B9), 16239–16256. https://doi.org/10.1029/93jb00888

Pognante, U., Rösli, U., & Toscani, L. (1985). Petrology of ultramafic and mafic rocks from the lanzo peridotite body (western Alps). *Lithos*, *18*, 201–214. https://doi.org/10.1016/0024-4937(85)90025-8

Poulaki, E. M., & Stockli, D. F. (2022). The paleotectonic evolution of the western mediterranean: Provenance insights from the internal Betics, southern Spain. *Frontiers in Earth Science*, *10*, 929502. https://doi.org/10.3389/feart.2022.929502

Poulaki, E. M., Stockli, D. F., Flansburg, M. E., & Soukis, K. (2019). Zircon u-pb chronostratigraphy and provenance of the Cycladic Blueschist Unit and the nature of the contact with the Cycladic Basement on Sikinos and Ios Islands, Greece. *Tectonics*, *38*(10), 3586–3613. https://doi.org/10.1029/2018tc005403

Poulaki, E. M., Stockli, D. F., & Shuck, B. D. (2023). Pre-subduction architecture controls coherent underplating during subduction and exhumation (Nevado-Filábride Complex, southern Spain). *Geochemistry, Geophysics, Geosystems*, *24*(3), e2022GC010802. https://doi.org/10.1029/2022gc010802

Rajič, K., Raimbourg, H., Famin, V., Moris-Muttoni, B., Fisher, D. M., Morell, K. D., & Canizarés, A. (2023). Exhuming an accretionary prism: A case study of the Kodiak accretionary complex, Alaska, USA. *Tectonics*, *42*(10), e2023TC007754. https://doi.org/10.1029/2023tc007754

Ranero, C. R., Phipps Morgan, J., McIntosh, K., & Reichert, C. (2003). Bending-related faulting and mantle serpentinization at the middle America Trench. *Nature*, *425*(6956), 367–373. https://doi.org/10.1038/nature01961

Reinecke, T. (1998). Prograde high-to ultrahigh-pressure metamorphism and exhumation of oceanic sediments at lago di cignana, zermatt-saas zone, western alps. *Lithos*, *42*(3–4), 147–189. https://doi.org/10.1016/s0024-4937(97)00041-8

Ring, U., & Layer, P. W. (2003). High-pressure metamorphism in the Aegean, eastern Mediterranean: Underplating and exhumation from the late cretaceous until the miocene to recent above the retreating hellenic subduction zone. *Tectonics*, *22*(3). https://doi.org/10.1029/2001tc001350

Ring, U., Will, T., Glodny, J., Kumerics, C., Gessner, K., Thomson, S., et al. (2007). Early exhumation of high-pressure rocks in extrusion wedges: Cycladic blueschist unit in the eastern Aegean, Greece, and Turkey. *Tectonics*, *26*(2). https://doi.org/10.1029/2005tc001872

Roda, M., Spalla, M. I., & Marotta, A. M. (2012). Integration of natural data within a numerical model of ablative subduction: A possible interpretation for the alpine dynamics of the austroalpine crust. *Journal of Metamorphic Geology*, *30*(9), 973–996. https://doi.org/10.1111/jmg.12000

Rose, I., Buffett, B., & Heister, T. (2017). Stability and accuracy of free surface time integration in viscous flows. *Physics of the Earth and Planetary Interiors*, *262*, 90–100. https://doi.org/10.1016/j.pepi.2016.11.007

Royden, L. H., & Husson, L. (2009). Subduction with variations in slab buoyancy: Models and application to the banda and apennine systems. In *Subduction zone geodynamics* (pp. 35–45). Springer.

Rubatto, D., & Scambelluri, M. (2003). U-pb dating of magmatic zircon and metamorphic baddeleyite in the ligurian eclogites (Voltri Massif, western Alps). *Contributions to Mineralogy and Petrology*, *146*(3), 341–355. https://doi.org/10.1007/s00410-003-0502-x

Ruh, J. B. (2020). Numerical modeling of tectonic underplating in accretionary wedge systems. *Geosphere*, *16*(6), 1385–1407. https://doi.org/10.1130/ges02273.1

Ruh, J. B., Le Pourhiet, L., Agard, P., Burov, E., & Gerya, T. (2015). Tectonic slicing of subducting oceanic crust along plate interfaces: Numerical modeling. *Geochemistry, Geophysics, Geosystems*, *16*(10), 3505–3531. https://doi.org/10.1002/2015gc005998

Sample, J. C., & Moore, J. C. (1987). Structural style and kinematics of an underplated slate belt, Kodiak and adjacent islands, Alaska. *Geological Society of America Bulletin*, *99*(1), 7–20. https://doi.org/10.1130/0016-7606(1987)99<7:ssakoa>2.0.co;2

Schellart, W., Stegman, D., Farrington, R., & Moresi, L. (2011). Influence of lateral slab edge distance on plate velocity, trench velocity, and subduction partitioning. *Journal of Geophysical Research*, *116*(B10), B10408. https://doi.org/10.1029/2011jb008535

Schmidt, W. L., & Platt, J. P. (2022). Stress, microstructure, and deformation mechanisms during subduction underplating at the depth of tremor and slow slip, Franciscan complex, northern California. *Journal of Structural Geology*, *154*, 104469. https://doi.org/10.1016/j.jsg.2021.104469

Schneider, J., Bosch, D., Monie, P., Guillot, S., García-Casco, A., Lardeaux, J.-M., et al. (2004). Origin and evolution of the escambray massif (central Cuba): An example of HP/LT rocks exhumed during intraoceanic subduction. *Journal of Metamorphic Geology*, *22*(3), 227–247. https://doi.org/10.1111/j.1525-1314.2004.00510.x

Schubert, G., Froidevaux, C., & Yuen, D. (1976). Oceanic lithosphere and asthenosphere: Thermal and mechanical structure. *Journal of Geophysical Research*, *81*(20), 3525–3540. https://doi.org/10.1029/jb081i020p03525

Sdrolias, M., & Müller, R. D. (2006). Controls on back-arc basin formation. *Geochemistry, Geophysics, Geosystems*, *7*(4). https://doi.org/10.1029/2005gc001090

Shreve, R. L., & Cloos, M. (1986). Dynamics of sediment subduction, melange formation, and prism accretion. *Journal of Geophysical Research*, *91*(B10), 10229–10245. https://doi.org/10.1029/jb091ib10p10229

Sizova, E., Gerya, T., Brown, M., & Perchuk, L. (2010). Subduction styles in the Precambrian: Insight from numerical experiments. *Lithos*, *116*(3–4), 209–229. https://doi.org/10.1016/j.lithos.2009.05.028

Smye, A. J., & England, P. C. (2023). Metamorphism and deformation on subduction interfaces: 2. Petrological and tectonic implications. *Geochemistry, Geophysics, Geosystems*, *24*(1), e2022GC010645. https://doi.org/10.1029/2022gc010645

Stegman, D., Freeman, J., Schellart, W. P., Moresi, L., & May, D. (2006). Influence of trench width on subduction Hinge retreat rates in 3-d models of slab rollback. *Geochemistry, Geophysics, Geosystems*, *7*(3). https://doi.org/10.1029/2005gc001056

Stöckhert, B. (2002). Stress and deformation in subduction zones: Insight from the record of exhumed metamorphic rocks. *Geological Society, London, Special Publications*, *200*(1), 255–274. https://doi.org/10.1144/gsl.sp.2001.200.01.15

Stöckhert, B., & Gerya, T. V. (2005). Pre-collisional high pressure metamorphism and nappe tectonics at active continental margins: A numerical simulation. *Terra Nova*, *17*(2), 102–110. https://doi.org/10.1111/j.1365-3121.2004.00589.x

Stoner, R., Holt, A., Epstein, G., Guevara, V., & Condit, C. (2025). Emergent feedbacks between progressive serpentinization, interface weakening, and subduction rates. *Geochemistry, Geophysics, Geosystems*, *26*(11), e2025GC012488. https://doi.org/10.1029/2025gc012488

Syracuse, E. M., van Keken, P. E., & Abers, G. A. (2010). The global range of subduction zone thermal models. *Physics of the Earth and Planetary Interiors*, *183*(1–2), 73–90. https://doi.org/10.1016/j.pepi.2010.02.004

Tagami, T., Hasebe, N., & Shimada, C. (1995). Episodic exhumation of accretionary complexes: Fission-track thermochronologic evidence from the shimanto belt and its vicinities, southwest Japan. *Island Arc*, *4*(3), 209–230. https://doi.org/10.1111/j.1440-1738.1995.tb00144.x

Takeshita, T., Imayama, T., Ando, M., Kimura, Y., & Python, M. (2023). Pressure–temperature paths of tectonic blocks in mélange: Recording thermal evolution of a subduction channel at an initial stage of subduction. *Journal of Metamorphic Geology*, *41*(6), 787–816. https://doi.org/10.1111/jmg.12718

Tan, E., Lavier, L. L., Van Avendonk, H. J., & Heuret, A. (2012). The role of frictional strength on plate coupling at the subduction interface. *Geochemistry, Geophysics, Geosystems*, *13*(10). https://doi.org/10.1029/2012gc004214

Tewksbury-Christle, C. M., Behr, W. M., & Helper, M. A. (2021). Tracking deep sediment underplating in a fossil subduction margin: Implications for interface rheology and mass and volatile recycling. *Geochemistry, Geophysics, Geosystems*, *22*(3), e2020GC009463. https://doi.org/10.1029/2020gc009463

Tokle, L., Hirth, G., & Behr, W. M. (2019). Flow laws and fabric transitions in wet quartzite. *Earth and Planetary Science Letters*, *505*, 152–161. https://doi.org/10.1016/j.epsl.2018.10.017

Tulley, C. J., Fagereng, Å., & Ujiie, K. (2020). Hydrous oceanic crust hosts megathrust creep at low shear stresses. *Science Advances*, *6*(22), eaba1529. https://doi.org/10.1126/sciadv.aba1529

Turino, V., Holt, A., Neuharth, D., Stoner, R., & Behr, W. (2026). Interface deformation, exhumation, and underplating: The role of plate velocity changes throughout a subduction zone's lifetime. *Zenodo*. https://doi.org/10.5281/zenodo.18249159

Turino, V., & Holt, A. F. (2024). Spatio-temporal variability in slab temperature within dynamic 3-d subduction models. *Geophysical Journal International*, *236*(3), 1484–1498. https://doi.org/10.1093/gji/ggad489

Ujiie, K., Nishiyama, N., Yamamoto, H., Yamashita, M., Nagaya, T., Sano, T., & Kouketsu, Y. (2024). Duplex underplating, sediment dehydration and quartz vein mineralization in the deep tremor source region. *Journal of Geophysical Research: Solid Earth*, *129*(2), e2023JB027901. https://doi.org/10.1029/2023jb027901

Van Dinther, Y., Morra, G., Funiciello, F., Rossetti, F., & Faccenna, C. (2012). Exhumation and subduction erosion in orogenic wedges: Insights from numerical models. *Geochemistry, Geophysics, Geosystems*, *13*(6). https://doi.org/10.1029/2011gc004011

Van Keken, P. E., Hacker, B. R., Syracuse, E. M., & Abers, G. A. (2011). Subduction factory: 4. Depth-dependent flux of H_2O from subducting slabs worldwide. *Journal of Geophysical Research*, *116*(B1), B01401. https://doi.org/10.1029/2010jb007922

van Keken, P. E., Wada, I., Abers, G. A., Hacker, B. R., & Wang, K. (2018). Mafic high-pressure rocks are preferentially exhumed from warm subduction settings. *Geochemistry, Geophysics, Geosystems*, *19*(9), 2934–2961. https://doi.org/10.1029/2018gc007624

Vaughan-Hammon, J. D., Candioti, L. G., Duretz, T., & Schmalholz, S. M. (2022). Metamorphic facies distribution in the western alps predicted by petrological-thermomechanical models of syn-convergent exhumation. *Geochemistry, Geophysics, Geosystems*, *23*(8), e2021GC009898. https://doi.org/10.1029/2021gc009898

Von Herzen, R., Ruppel, C., Molnar, P., Nettles, M., Nagihara, S., & Ekström, G. (2001). A constraint on the shear stress at the Pacific-Australian plate boundary from heat flow and seismicity at the kermadec forearc. *Journal of Geophysical Research*, *106*(B4), 6817–6833. https://doi.org/10.1029/2000jb900469

Wakabayashi, J. (2015). Anatomy of a subduction complex: Architecture of the Franciscan Complex, California, at multiple length and time scales. *International Geology Review*, *57*(5–8), 669–746. https://doi.org/10.1080/00206814.2014.998728

Wang, Y., Wang, K., He, J., & Zhang, L. (2023). On unusual conditions for the exhumation of subducted oceanic crustal rocks: How to make rocks hotter than models. *Earth and Planetary Science Letters*, *615*, 118213. https://doi.org/10.1016/j.epsl.2023.118213

Wang, Y., Zhang, L.-F., Li, Z.-H., Li, Q.-Y., & Bader, T. (2019). The exhumation of subducted oceanic-derived eclogites: Insights from phase equilibrium and thermomechanical modeling. *Tectonics*, *38*(5), 1764–1797. https://doi.org/10.1029/2018tc005349

Warren, C. J., Beaumont, C., & Jamieson, R. A. (2008). Formation and exhumation of ultra-high-pressure rocks during continental collision: Role of detachment in the subduction channel. *Geochemistry, Geophysics, Geosystems*, *9*(4). https://doi.org/10.1029/2007gc001839

Whitney, D. L., & Davis, P. B. (2006). Why is lawsonite eclogite so rare? Metamorphism and preservation of lawsonite eclogite, Sivrihisar, Turkey. *Geology*, *34*(6), 473–476. https://doi.org/10.1130/g22259.1

Willner, A., Glodny, J., Gerya, T., Godoy, E., & Massonne, H.-J. (2004). A counterclockwise ptt path of high-pressure/low-temperature rocks from the coastal cordillera accretionary complex of south-central Chile: Constraints for the earliest stage of subduction mass flow. *Lithos*, *75*(3–4), 283–310.

Wintsch, R., Byrne, T., & Toriumi, M. (1999). Exhumation of the sanbagawa blueschist belt, SW Japan, by lateral flow and extrusion: Evidence from structural kinematics and retrograde PTT paths. *Geological Society, London, Special Publications*, *154*(1), 129–155. https://doi.org/10.1144/gsl.sp.1999.154.01.06

Yamato, P., Agard, P., Burov, E., Le Pourhiet, L., Jolivet, L., & Tiberi, C. (2007). Burial and exhumation in a subduction wedge: Mutual constraints from thermomechanical modeling and natural P-T-t data (Schistes Lustrés, western Alps). *Journal of Geophysical Research*, *112*(B7). https://doi.org/10.1029/2006jb004441

Yáñez, G., & Cembrano, J. (2004). Role of viscous plate coupling in the late Tertiary Andean tectonics. *Journal of Geophysical Research*, *109*(B2). https://doi.org/10.1029/2003jb002494